



## Review of functional titanium oxides. I: TiO<sub>2</sub> and its modifications

Nazanin Rahimi, Randolph A. Pax, Evan MacA. Gray\*

Queensland Micro- and Nanotechnology Centre, Griffith University, QLD 4111, Brisbane, Australia



### ARTICLE INFO

#### Article history:

Available online 3 August 2016

#### Keywords:

TiO<sub>2</sub> polymorphs  
Properties  
Modifications  
DFT  
Photocatalysis

### ABSTRACT

An extensive and wide-ranging literature about the polymorphs of titanium dioxide (TiO<sub>2</sub>) has accumulated during the last few decades, providing a very large resource of data on its properties, functionality and many present and potential industrial uses. This review focuses on the structural, kinetic, thermodynamic and electrical properties of TiO<sub>2</sub> from the viewpoint of the relationship between the crystal structure and its present or potential useful functionality, via the electronic structure. The reason for this focus is the fundamental relationship between the electronic band structure of this wide band-gap semiconductor and its interaction with light and chemical species. Intense interest in the photoactivity of TiO<sub>2</sub> followed the demonstration by Fujishima and Honda in 1972 of its ability to dissociate water using sunlight. Approaches to band gap engineering via chemical modifications are surveyed and correlated with band-structure calculations using Density Functional Theory and Hartree Fock methods. In the last section, progress in TiO<sub>2</sub> applications and prospects for new applications of this material are summarised.

© 2016 Elsevier Ltd. All rights reserved.

### Contents

1. Introduction .....	87
2. Preparation and characterization .....	87
3. Properties of TiO <sub>2</sub> .....	91
3.1. Structure .....	91
3.2. Kinetic and thermodynamic properties .....	92
3.3. Electrical and optical properties .....	93
4. Modifications .....	96
4.1. Noble metal loading .....	96
4.2. Ion doping .....	97
4.2.1. Cation-doped TiO <sub>2</sub> .....	98
4.2.2. Anion-doped TiO <sub>2</sub> .....	98
4.2.3. Oxygen-deficient TiO <sub>2</sub> .....	99
4.3. Ion implantation .....	100
5. Research progress in applications .....	101
5.1. UV absorption .....	101
5.2. Photocatalysis .....	101
5.2.1. Photocatalytic water splitting .....	101
6. Summary .....	102
References .....	103

\* Corresponding author.

E-mail address: [e.gray@griffith.edu.au](mailto:e.gray@griffith.edu.au) (E.MacA. Gray).

## List of abbreviations

AFM	Atomic Force Microscopy
CB	Conduction Band
DFT	Density Functional Theory
DOS	Density of States
FLAPW	Full-Potential Linearized Augmented Plane Wave
GGA	Generalized Gradient Approximation
HF	Hartree-Fock
LCAO	Linear Combination of Atomic Orbitals
LDA	Local Density Approximation
LMTO	Linear Muffin-Tin Orbital
NHE	Normal Hydrogen Electrode
PTFE	Polytetrafluoroethylene
SPF	Sun Protection Factor
TEM	Transmission Electron Microscopy
VB	Valence Band
WBS	Wide Band-gap Semiconductor
XRD	X-Ray Diffraction

## 1. Introduction

$\text{TiO}_2$  was singled out as an important oxide material in the wide-ranging review of future directions in solid state chemistry by Cava et al. [1] for the US National Science Foundation. It was seen to have general relevance to Earth science and fundamental solid state chemistry, and particular relevance to photovoltaic/photo-electrochemical cells. The fruitful connection between solid state chemistry and condensed matter physics was said to be in its infancy. Especially from the viewpoint of this review, in which we emphasise the origins of functionality in band structure, that connection has strengthened greatly, evidenced by the number of references to publications in condensed matter physics.

$\text{TiO}_2$ , the naturally occurring oxide of titanium, was discovered in 1795, and its commercial production started in the 1920s [2]. About 95% of titanium ore is processed into titanium dioxide, which is the most widely used titanium product. The global  $\text{TiO}_2$  market was valued at US\$13.14 billion in 2013 and is anticipated to reach US\$17.12 billion by 2020, with a market rise of 8.0 million tonnes annually. The Asia-Pacific region dominated the global titanium dioxide market with a share of over 40% in 2013 [3].

$\text{TiO}_2$  has been utilized in numerous commercial applications including as an opacifying agent in paints, plastics, paper textiles and inks, corrosion-resistant coatings, anti-bacterial agents, water and air purification, self-cleaning surfaces, food additives and as an ultra-violet absorber in cosmetic products [4–9]. In addition to its current use in industry,  $\text{TiO}_2$  has been extensively studied for applications in water remediation, photocatalysis, rechargeable batteries, super capacitors and sensor devices etc. [10–12]. The functional performance of  $\text{TiO}_2$  is fundamentally determined by its electronic structure. Its properties in the visible and UV portions of the electromagnetic spectrum are especially significant.

$\text{TiO}_2$  is a simple inorganic compound existing in four fundamental crystal forms (space groups): anatase ( $I4_1/\text{amd}$ ), rutile ( $P4_2/\text{mnm}$ ), brookite ( $Pbca$ ) and  $\text{TiO}_2(\text{B})$  ( $C2/\text{m}$ ). Furthermore, the  $\text{TiO}_2$  phase diagram is rich at elevated pressures, including high pressure phases thought by geologists to be candidates for the minerals in the Earth's mantle. Columbite ( $Pbcn$ ), baddeleyite ( $P2_1/\text{c}$ ), cotunnite ( $Pnma$ ), pyrite and fluorite structures are high pressure polymorphs of  $\text{TiO}_2$  [13–23].

Rutile is the most stable phase at ambient pressure and temperature in macroscopic sizes while anatase is more stable in

nanoscopic sizes [24,25]. The more compact structure of rutile relative to anatase causes important differences in physical properties. Rutile has a higher refractive index, higher specific gravity and greater chemical stability than anatase. Rutile melts at 1825 °C while anatase irreversibly transforms to rutile beginning at about 500 °C. Brookite is the rarest naturally occurring form of  $\text{TiO}_2$  and is difficult to produce in pure form. Brookite has the same colour and lustre as rutile. Its hardness and density are nearly the same as those of rutile.  $\text{TiO}_2(\text{B})$  is less well known than rutile, anatase and brookite.  $\text{TiO}_2(\text{B})$  was synthesized in 1980 by Marchand et al. [26], and found in nature by Banfield et al. [27]. “B” in  $\text{TiO}_2(\text{B})$  stands for bronze, by analogy with the tungsten bronze compounds.  $\text{TiO}_2(\text{B})$  is the least dense of the four natural polymorphs of  $\text{TiO}_2$ , so it seems to be an excellent host for Li intercalation in comparison with the other polymorphs [26,28]. However, because of its metastable properties, only a few investigations have been carried out in the electrochemistry field.

Titanium-based pigment is by far the largest end-use of titanium feedstocks, accounting for over 50% of the market share. For rutile a particle size of around 0.25 microns yields the highest scattering efficiency across the whole visible spectrum, while the ideal particle size for anatase is around 0.3 microns. Nanoscale titanium dioxide is approximately 100 times smaller than commercial  $\text{TiO}_2$  pigments and has different physical properties. Nanoscopic  $\text{TiO}_2$  is used in sunscreens to attenuate both the UVB (290–320 nm) and UVA (320–400 nm) sorption of the solar spectrum [5]. Since Fujishima and Honda [29] studied  $\text{TiO}_2$  as a photocatalyst to split water to hydrogen and oxygen in 1972, it has gained significant attention, and attempts have been made to improve its catalytic performance. The biggest barrier to using  $\text{TiO}_2$  as a photo-activated catalyst is its large energy gap between the conduction and valence bands. Excitation of electrons across this wide band gap is possible for only 3–4% of the air-mass 1.0 solar spectrum. Therefore, many attempts have been made to reduce the  $\text{TiO}_2$  band gap so as to operate effectively with visible light. Lowering the band gap of  $\text{TiO}_2$  is also expected to pave the way to applications in the renewable energy sector, including photovoltaic cells and hydrogen production by photo catalysis [30].

There are numerous methods of modifying titanium dioxide to alter its electronic structure, including annealing at high temperatures, anion/cation doping, implantation, dye-sensitization etc. In this review, the focus is on the functional properties of modified  $\text{TiO}_2$  and their relationship to crystal structure, kinetic and thermodynamic properties and especially, electronic structure. For the prior state of knowledge about  $\text{TiO}_2$ , the reader is referred to the very wide-ranging review by Diebold [31], to the review of photocatalysis-related phenomena, emphasizing those related to environmentally hazardous compounds, by Carp et al. [32], and to the review of photocalalysis and related surface phenomena by Jujishima et al. [33]. These very comprehensive papers concentrate on phenomenology, whereas our aim is to examine the link between structure and function as increasingly revealed by the modern theoretical tools that have become readily available and more reliable in the intervening decade or so. Companion reviews by the present authors will provide more detail about oxygen-deficient  $\text{TiO}_2$  and Ti-based Magnéli phases from a similar viewpoint. Because of their high surface area and short internal diffusion paths, nanoscopic  $\text{TiO}_2$  and its modifications, now becoming readily available commercially, are of special interest.

## 2. Preparation and characterization

Titanium dioxide micro- and nanoparticles have been synthesized via hydrolysis, sol-gel, micro-emulsion or reverse micelles,

flame pyrolysis, solvo/hydrothermal, chemical vapour deposition and physical vapour deposition. Among these techniques hydrolysis is preferable because its operating conditions are the closest to ambient temperature and pressure. Anatase and rutile are commonly synthesized by hydrolysis of titanium compounds such as titanium tetrachloride, titanium sulfate or titanium alkoxides in water solution. Producing the pure brookite phase is a difficult process, so most of the studies have reported the synthesis process for the mixture of brookite, rutile and/or anatase phases.  $\text{TiO}_2(\text{B})$  was prepared by hydrolysis of  $\text{K}_2\text{Ti}_4\text{O}_9$  followed by heating at  $500^\circ\text{C}$  [26].

Relatively macroscopic  $\text{TiO}_2$  is produced industrially by chloride and sulfate processes [34,35]. The chloride process is generally lower in cost and produces a higher quality product due to the inherent purity of the rutile ore. In contrast, using low-grade ilmenite ore in the sulfate process leads to a higher production cost per tonne of  $\text{TiO}_2$ .

Alkoxide is another precursor which has been used for producing different phases of  $\text{TiO}_2$  in aqueous solutions of variety acids and bases. Metal alkoxide is usually used as a precursor in the sol–gel method, which produces fine, spherically shaped powders with uniform size  $<1.0$  mm. The high price of the alkoxide has limited the commercialization of this method [36].

Template synthesis has been used for preparation of a variety of micro- and nano-materials. In this process a desired material is synthesized within the pores of “track-etch” polymeric membranes and porous alumina membranes. In this method, desired nano-materials are prepared in cylindrical pores of uniform diameter [37]. There are five recognized chemical strategies to conduct template synthesis within the alumina and polymeric template membranes: electrochemical deposition, electroless deposition, chemical polymerization, sol–gel deposition and chemical vapour deposition (CVD) [38].

In 1998, Kasuga et al. [39] reported a simple method for the preparation of  $\text{TiO}_2$  nanotubes, without the use of sacrificial templates. This method could be used after the sol–gel process to convert the derived fine  $\text{TiO}_2$ -based powders to nanotubes by treatment of amorphous  $\text{TiO}_2$  for 20 h at  $110^\circ\text{C}$  with a 5–10 M NaOH aqueous solution in a PTFE-lined batch reactor [39].

Among the three most utilised  $\text{TiO}_2$  polymorphs, anatase at small particle sizes is the most stable phase, but rutile becomes the most stable phase under ambient conditions as the particle size increases beyond  $\sim 14$  nm [40]. Ding et al. [41] reported that the anatase-to-rutile transformation reaction rate decreases with grain growth of nanoparticles. During the annealing process some anatase particles convert to rutile and others agglomerates to larger particle sizes. Therefore, the efficiency of phase transition decreases with time, and the grain growth process rate increases by anatase-to-rutile transformation [41]. The anatase-rutile transformation kinetics is size-dependent and proceeds faster with decreasing particle size.

Thermoanalytical techniques have been used to characterize the phase transformation process. Ye et al. analysed the structural transition of nanocrystalline brookite-based  $\text{TiO}_2$  through TG-DTA (thermogravimetry/differential thermal analysis). They observed two endothermic peaks in the DTA curve which correspond to desorption of physi- and chemisorbed species and the structural phase transformation of brookite to anatase then to rutile, respectively [42,43].

Mehranpour et al. worked on the phase transformation kinetics of  $\text{TiO}_2$  nanoparticles (50 nm) prepared by the sol–gel method. The XRD studies in the temperature range of 200–800 °C show that the anatase–rutile phase transition starts at temperatures lower than 200 °C. They concluded that the faster phase transition of the prepared sample is because of the better size uniformity and shape of the sample [44].

The common polymorphs of  $\text{TiO}_2$  are readily distinguishable by XRD and Raman spectroscopy. XRD ( $\text{Cu K}\alpha$  radiation) patterns of the three common structural modifications of  $\text{TiO}_2$  nanoparticles, prepared by hydrothermal treatment, are shown in Fig. 1 [45,46]. In addition, the XRD patterns for different nanocrystallite sizes of rutile and anatase phases are shown in Figs. 2 and 3.

Cheng et al. [49] synthesised uniform nano-sized rutile and studied the produced nanoparticles by Raman spectroscopy. They reported that the Raman peaks of smaller particles were broader and less intense than those of bigger nanoparticles. A new broad band was also detected at ca.  $112\text{ cm}^{-1}$  in the smaller particles. Swamy et al. confirmed the observation of the additional low frequency band at ca.  $105\text{ cm}^{-1}$  which was attributed to a surface vibrational mode as shown in Fig. 4 [47].

The Raman spectra of natural brookite crystals from Switzerland and Brazil and a synthetic brookite were compared by Tompsett et al. There is a characteristic intense band at  $153\text{ cm}^{-1}$  (Fig. 5). In contrast, anatase has a band of similar intensity at  $144\text{ cm}^{-1}$  and rutile lacks a strong band in this region [50].

Fig. 6 shows the Raman spectra of brookite in parallel (XX, YY, ZZ) configurations using different excitation laser lines. The authors observed two missing modes of the Tompsett et al. brookite Raman spectra (seven  $\text{A}_{1g}$  modes at 125, 152, 194, 246, 412, 492, and  $640\text{ cm}^{-1}$ ) at 324 and  $545\text{ cm}^{-1}$  [51].

Since the crystal phase significantly affects the properties of nanocrystals, phase control and the process of phase transformation of anatase-to-rutile and brookite has been well investigated during the last decades [69]. Particle size is a determining factor in the phase transition sequence of anatase-to-rutile and brookite-to-rutile because of sized-dependent thermodynamic stability of  $\text{TiO}_2$  nanoparticles. In 2000 Zhang and Banfield [52] did a comprehensive study on the phase transformation behaviour of  $\text{TiO}_2$  nanocrystals isothermally (at 723, 853, and 973 K) and isochronally (in the temperature range of 598–1023 K). They studied the enthalpy change of  $\text{TiO}_2$  polymorphs with respect to the particle size. Regarding the fact that surface energy alters with particle size, they concluded that for the same particle sizes, anatase is the most thermodynamically stable phase at sizes less than 11 nm, between 11 and 35 nm brookite is the most stable and for the particle sizes greater than 35 nm, rutile is the most stable

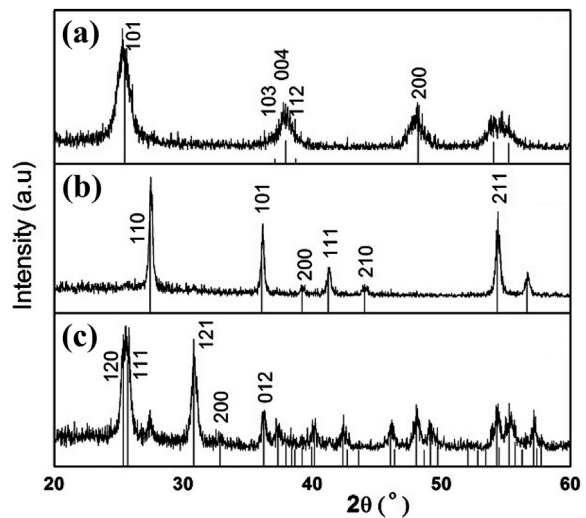


**Fig. 1.** XRD ( $\text{Cu K}\alpha$  radiation) patterns of  $\text{TiO}_2$  nanoparticles prepared by hydrothermal treatment: (a) anatase, (b) rutile and (c) brookite. A small fraction of rutile (<5%) exists in the brookite phase [45].

(Reprinted with permission from Reyes-Coronado, D., G. Rodriguez-Gattorno, M. Espinosa-Pesqueira, C. Cab, R. De Coss, and G. Oskam. Nanotechnology, 2008. **19**(14): p. 145605. Copyright IOP Publishing, 2008.)

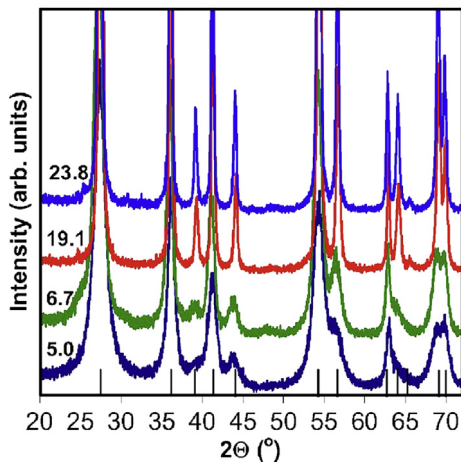


**Fig. 2.** XRD ( $\text{Cu K}\alpha$  radiation) patterns of nanosized-rutile  $\text{TiO}_2$  for different crystallite sizes. The short vertical bars at the bottom are reflection markers for bulk rutile [47]. (Reprinted with permission from Swamy, V., B.C. Muddle, and Q. Dai, Applied Physics Letters, 2006. **89**(16): p. 3118. Copyright American Institute of Physics, 2006.)

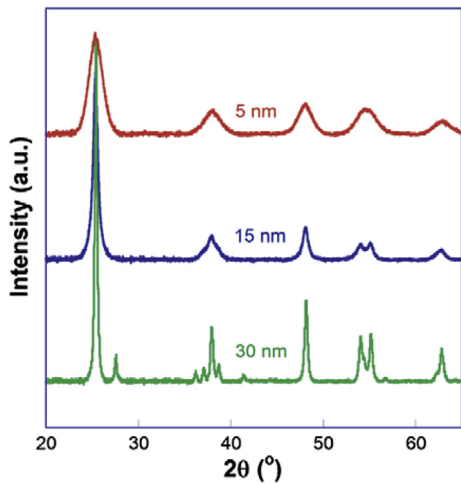


**Fig. 3.** XRD ( $\text{Cu K}\alpha$  radiation) pattern of nanosized-anatase  $\text{TiO}_2$  for different crystallite sizes [48].

(Reprinted with permission from Wang, J.W., A.K. Mishra, Q. Zhao, and L.P. Huang, Journal of Physics D-Applied Physics, 2013. **46**(25): p. 255303. Copyright IOP Publishing, 2013.)

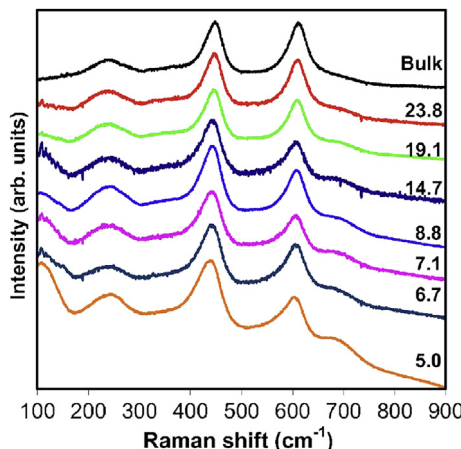


**Fig. 4.** Raman spectra of rutile  $\text{TiO}_2$  for indicated average size of nanoparticles [47]. (Reprinted with permission from Swamy, V., B.C. Muddle, and Q. Dai, Applied Physics Letters, 2006. **89**(16): p. 3118. Copyright American Institute of Physics, 2006.)

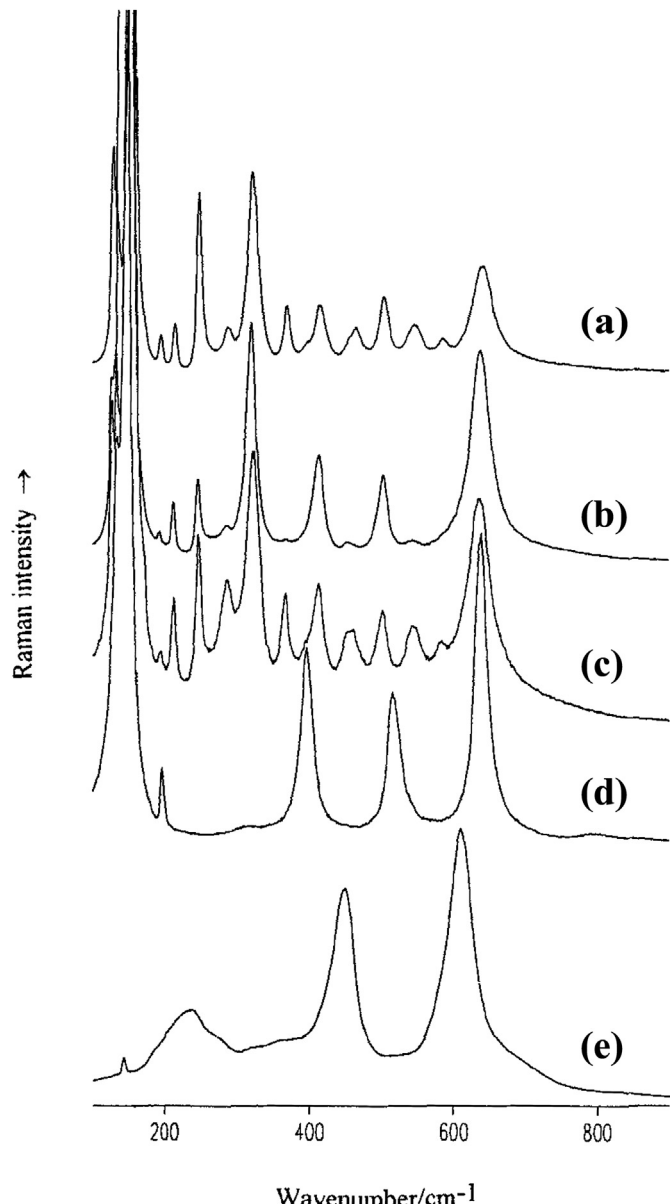


**Fig. 5.** Raman spectra from 100 to 900  $\text{cm}^{-1}$ : (a) brookite (010) face, Swiss brookite; (b) brookite (010) face, Brazilian brookite; (c) synthetic brookite; (d) synthetic anatase; (e) synthetic rutile [50].

(Reprinted with permission from Tompsett, G., G. Bowmaker, R. Cooney, J. Metson, K. Rodgers, and J. Seakins, Journal of Raman Spectroscopy, 1995. **26**(1): p. 57–62. Copyright John Wiley and Sons, 1995.)

phase. In addition to the particle size, temperature is another important factor which affects the phase transition reactions. In a relatively recent study, Zhang et al. [53] followed the phase transformation of anatase to rutile by XRD ( $\text{Cu K}\alpha$  radiation), UV-visible Raman spectroscopies and transmission electron microscopy (TEM). The TEM images of the  $\text{TiO}_2$  sample calcined at 500 °C revealed a particle-size range of 10–30 nm. During calcination by increasing the temperature to 800 °C, the particle size could increase to 200 nm. XRD and Raman spectroscopy measurements (Fig. 7) relate those agglomerations to the development of the anatase phase and to the anatase-to-rutile phase transition. Fig. 7a shows the XRD pattern of initially amorphous  $\text{TiO}_2$  at different calcination temperatures. The peaks of anatase are stronger and sharper below 500 °C. For higher calcination temperatures

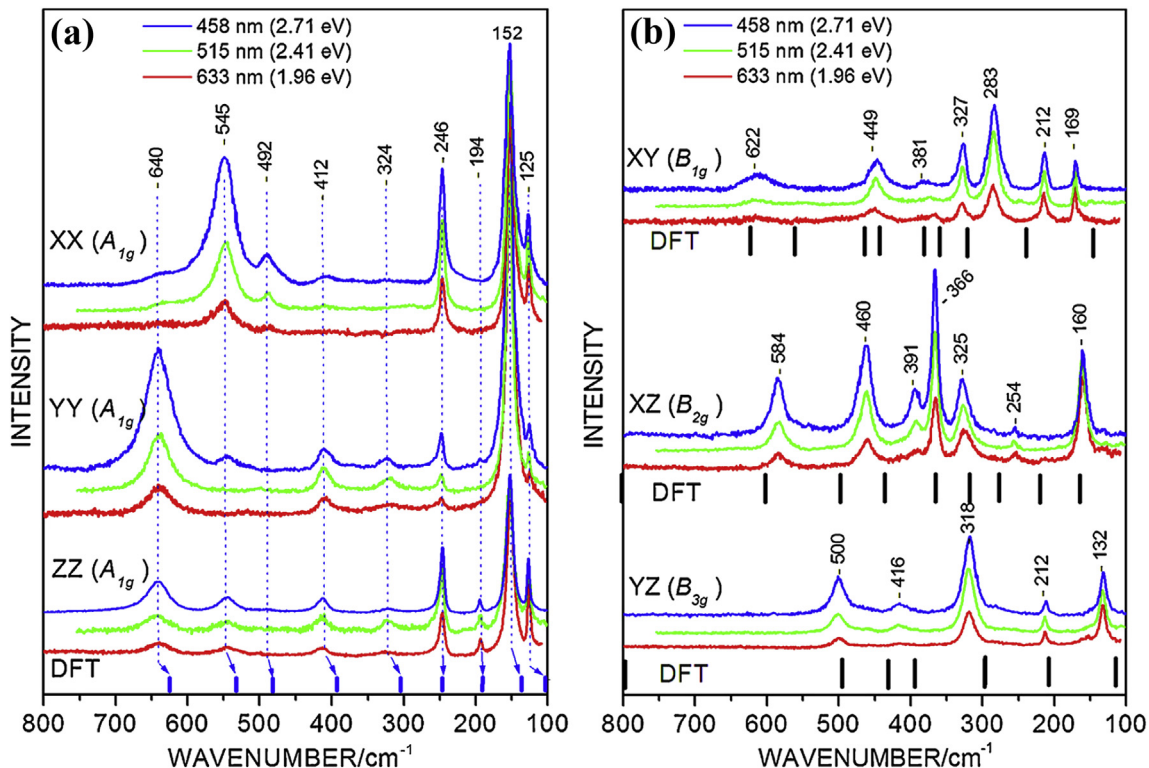


**Fig. 6.** Raman spectra of brookite at 300 K with 633 nm, 515 nm and 458 nm excitation. (a) A modes. (b) B modes. The DFT-calculated values are shown at the bottom of the plot [51]. (Reprinted with permission from Iliev, M., V. Hadjiev, and A. Litvinchuk, Vibrational Spectroscopy, 2013. **64**: p. 148–152. Copyright Elsevier Science, 2013.)

(>550 °C) the anatase peak intensities decrease and the peaks from rutile start to appear. The diffraction peaks of anatase completely disappear at 750 °C, showing that the transition to rutile is complete. The visible-Raman spectroscopy of initially amorphous TiO<sub>2</sub> is also shown in Fig. 7b, confirming the XRD results.

Zhu et al. [54] studied the effects of grain size and the phase content on the phase transition in the temperature range of 200–600 °C. Fig. 8 shows the XRD patterns of a prepared sample comprising anatase (grain size: 4.9 nm) and brookite (grain size: 5.8 nm) with average content 55.3 wt.% anatase. The brookite

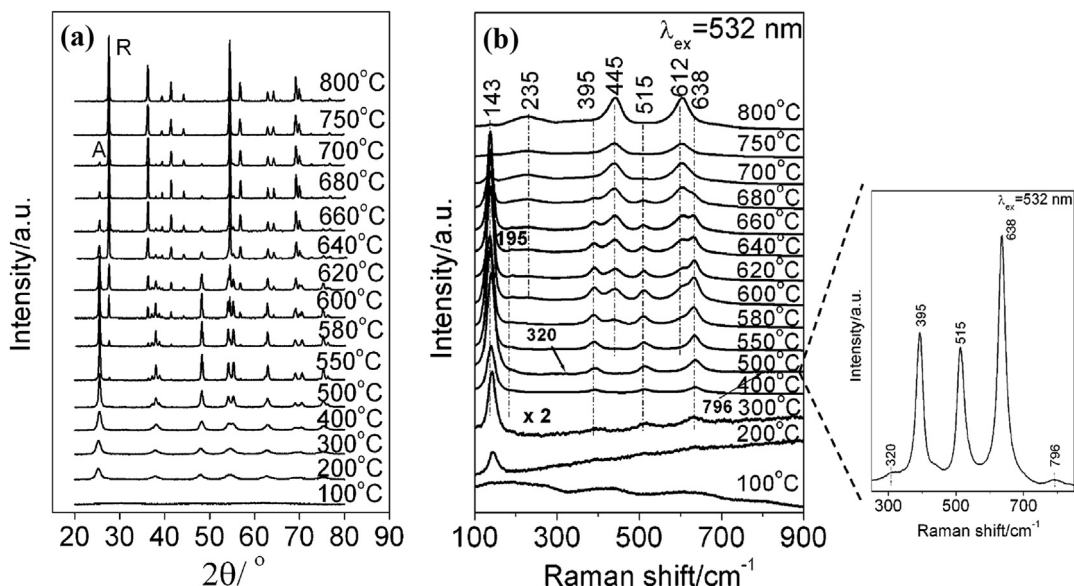


**Fig. 7.** (a) XRD (Cu K $\alpha$  radiation) patterns and (b) visible Raman spectra of TiO<sub>2</sub> calcined at different temperatures [53].

(Reprinted with permission from Zhang, J., M.J. Li, Z.C. Feng, J. Chen, and C. Li, Journal of Physical Chemistry B, 2006. **110**(2): p. 927–935. Copyright American Chemical Society, 2006.)

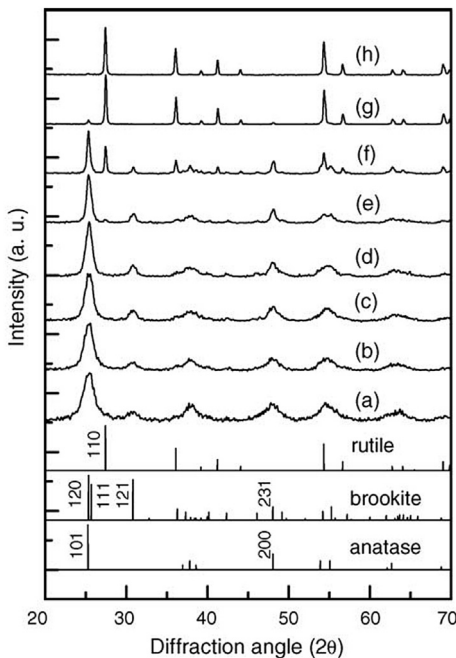


**Fig. 8.** XRD patterns of a sample includes 55.3 wt.% anatase annealed at various temperatures; (b–h) 200, 300, 400, 500, 550, 600 and 650 °C [54].  
(Reprinted with permission from Zhu, K.-R., M.-S. Zhang, J.-M. Hong, and Z. Yin, Materials Science and Engineering: A, 2005. **403**(1): p. 87–93. Copyright Elsevier, 2005.)

content of the sample starts to increase at 400 °C, reaching 55.4 wt.%, which demonstrates that anatase starts to transform to brookite before rutile. At higher temperatures (>500 °C) anatase and brookite transform to rutile directly.

Wang et al. [48] studied the phase transformation of anatase nanoparticles with initial size of 5 nm to rutile. They used a pyroprobe heater, for the first time, with ultra-fast heating to study sintering and phase transformation at the beginning of the process. They concluded that the transition rate is faster for the smaller particles, and the rutile-like structure evolves with time, initially at the interface between anatase nanoparticles and followed by growth of rutile nuclei. They also studied the anatase-to-rutile phase transition by Raman spectroscopy to explore the initial stage of the rutile-like structure production and they concluded that heat treatment of anatase nanoparticles at 600 °C initiates the production of rutile-like structural elements (Fig. 9) which evolve by heat treatment at 800 °C for 10 s.

### 3. Properties of TiO<sub>2</sub>

#### 3.1. Structure

Fig. 10 shows the crystal structure and building blocks of rutile, anatase and brookite. Fig. 11 shows the TiO<sub>6</sub> polyhedral representation of TiO<sub>2</sub>(B) [25]. Anatase and rutile have tetragonal structures and the brookite and TiO<sub>2</sub>(B) crystal systems are orthorhombic and monoclinic, respectively [35,45]. Anatase and rutile have common TiO<sub>6</sub> octahedron building blocks in a more or less distorted configuration. The octahedron structure is more distorted in anatase than rutile, see Fig. 10. In rutile the unit cell contains two TiO<sub>2</sub> units, and the Ti and O coordination numbers are six and three, respectively. On the other hand, the tetragonal unit cell of anatase has four TiO<sub>2</sub> units with the same coordination numbers of Ti and O as in rutile. The lattice parameters of the known titania phases are shown in Table 1. In both rutile and anatase there are two different

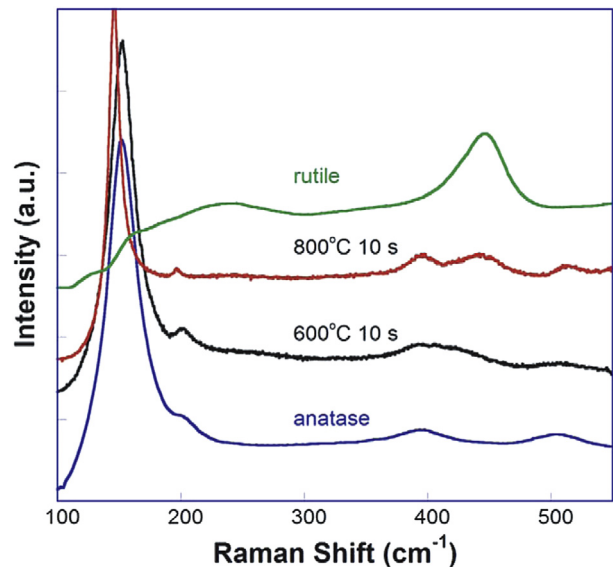


**Fig. 9.** Raman spectra of anatase nanoparticles with initial size of 5 nm after heating at 600 and 800 °C for 10 s [48].

(Reprinted with permission from Wang, J.W., A.K. Mishra, Q. Zhao, and L.P. Huang, Journal of Physics D-Applied Physics, 2013. **46**(25): p. 255303. Copyright IOP Publishing, 2013.)

lengths of titanium-oxygen bonds in each octahedron. Rutile has four Ti–O distances of  $1.946 \pm 0.003$  Å, and two of  $1.984 \pm 0.004$  Å. Anatase has also four Ti–O distances of  $1.937 \pm 0.003$  Å and two Ti–O distances of  $1.964 \pm 0.009$  Å [46]. Unit cell volumes of the polymorphs are:  $35.27$  Å<sup>3</sup> for TiO<sub>2</sub>(B),  $31.12$  Å<sup>3</sup> for rutile,  $32.20$  Å<sup>3</sup> for brookite and  $34.02$  Å<sup>3</sup> for anatase [26].

The surface structure of the rutile TiO<sub>2</sub>(110) surface has been well characterized. It consists of rows of bridging oxygen atoms that lie above the in-plane surface [55]. The ball-and-stick and space-filling models of the rutile TiO<sub>2</sub>(110) – (1 × 1) surface demonstrate the two-fold and three-fold-coordinated oxygen atoms (Figs. 12 and 13). The two-fold-coordinated ones are so-called bridging oxygen atoms which can easily be removed by thermal annealing due to their unsaturated coordination. The rows of bridging oxygen atoms are located directly on top of the 6-fold coordinated Ti rows [59–61].

Ramamoorthy and Vanderbilt [63] studied the shapes and surface energetics of titanium dioxide by the Wulff construction method. The calculated surface energies are shown in Table 2.

Regarding the calculations, the (110) surface has the lowest surface energy while the (001) is nearly unstable. The equilibrium shape of a macroscopic crystal of rutile is plotted in Fig. 14. The equilibrium shapes of the different structures depend on the synthesis conditions due to variations of the surface energy and surface tension in different environments [64,65]. The equilibrium shape of rutile in the Wulff construction consists of a tetragonal prism bounded by (110) and terminated by a pair of tetragonal pyramids bounded by (011). According to the results, the most stable surface among the rutile crystal facets is (110) [65].

From the Wulff construction and surface energies, the equilibrium shape of the anatase phase is shown in Fig. 15a [25], and compared to an anatase mineral crystal in Fig. 15 b. Fig. 16a and b shows the Wulff shape of brookite and TiO<sub>2</sub>(B) crystals [64,66]. The equilibrium crystal structure of brookite has seven different facets (Fig. 16a) [66]. A flat pseudo hexagonal prism constructed from (001), (100), (110) and (1̄10) is the equilibrium shape of TiO<sub>2</sub>(B), see Fig. 16b.

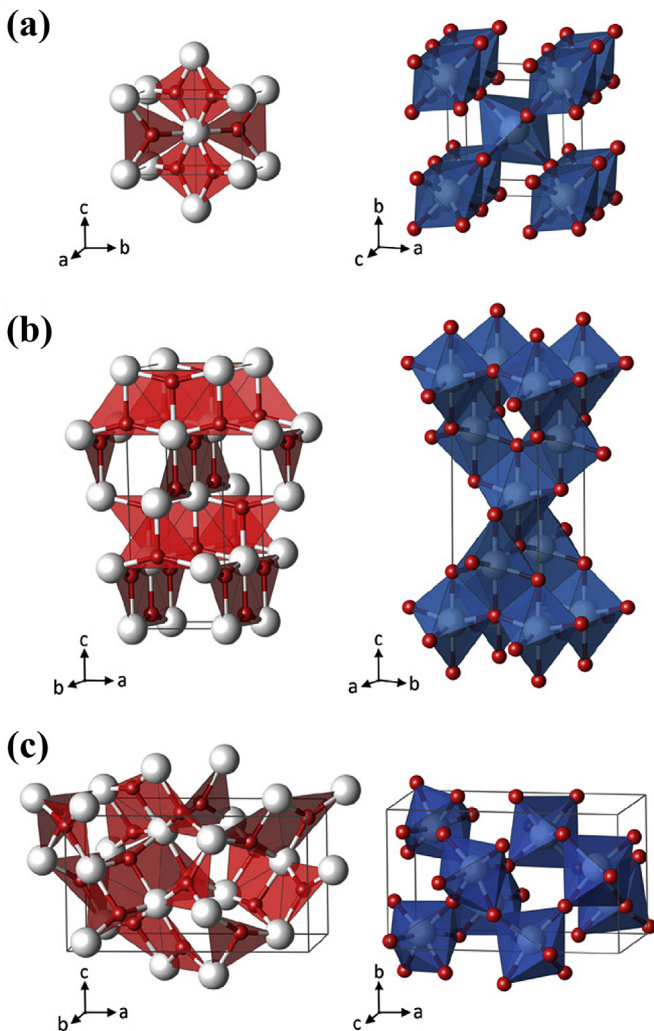


**Fig. 10.** Planar  $\text{Ti}_3\text{O}$  building-block representation (left) and  $\text{TiO}_6$  polyhedra (right) for the  $\text{TiO}_2$  phases rutile (a), anatase (b) and brookite (c) ( $\text{Ti}$  (white);  $\text{O}$  (red)). The experimental lattice parameters  $a = b = 4.5937 \text{ \AA}$ ;  $c = 2.9581 \text{ \AA}$  for rutile,  $a = b = 3.7842 \text{ \AA}$ ;  $c = 9.5146 \text{ \AA}$  for anatase and  $a = 9.16 \text{ \AA}$ ;  $b = 5.43 \text{ \AA}$ ;  $c = 5.13 \text{ \AA}$  for brookite [55]. (For interpretation of the references to colour in this figure legend, the reader is referred to the web version of this article.)

(Reprinted with permission from Landmann, M., E. Rauls, and W.G. Schmidt, J Phys Condens Matter, 2012. **24**(19): p. 195503. Copyright IOP Publishing, 2012.)

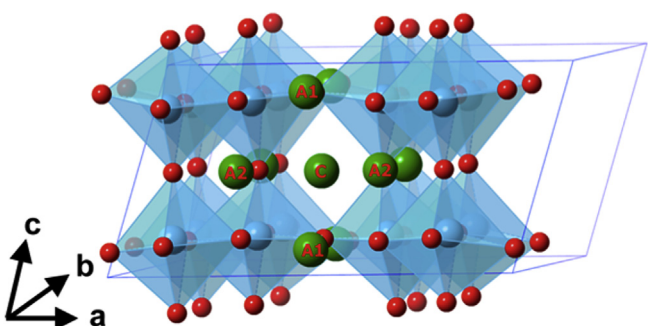


**Fig. 11.**  $\text{TiO}_6$  polyhedra for  $\text{TiO}_2(\text{B})$  phase [56].

(Reprinted with permission from Dylla, A.G., G. Henkelman, and K.J. Stevenson, Accounts of Chemical Research, 2013. **46**(5): p. 1104–1112. Copyright American Chemical Society, 2013.)

**Table 1**  
Experimental lattice parameters and band-gap energy of  $\text{TiO}_2$  polymorphs [26,45,58,59].

Phase	Crystal structure	Density ( $\text{g}/\text{cm}^3$ )	$a$ ( $\text{\AA}$ )	$b$ ( $\text{\AA}$ )	$c$ ( $\text{\AA}$ )	Band-gap energy (eV)
Rutile	Tetragonal	4.24	4.5937	4.5937	2.9581	3.0
Anatase	Tetragonal	3.83	3.7842	3.7842	9.5146	3.20
Brookite	Orthorhombic	3.17	9.16	5.43	5.13	3.26
$\text{TiO}_2(\text{B})$	Monoclinic	3.64	12.16	3.74	6.51	

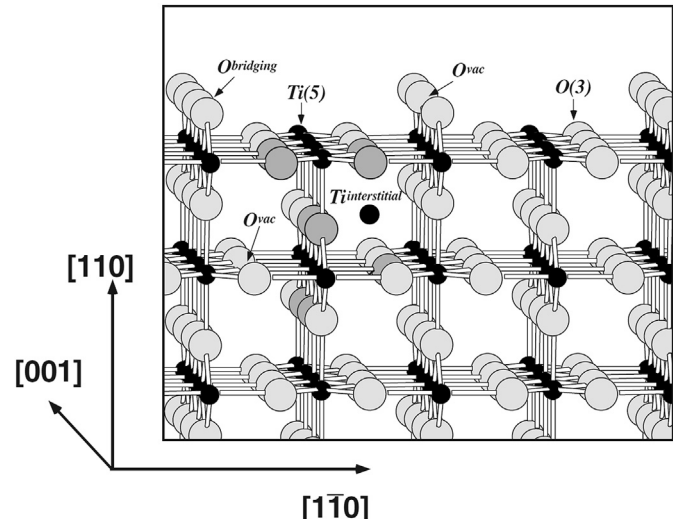


**Fig. 12.** Ball-and-stick model of the rutile  $\text{TiO}_2(110)$  –  $(1 \times 1)$  surface. Large light balls, oxygen; small black balls, titanium. Vacancies in bridging oxygen rows are common on vacuum-annealed surfaces. The two types of bulk defects that are prevalent in reduced  $\text{TiO}_2$  crystals, i.e. oxygen vacancies and titanium interstitials, are also indicated [61]. (Reprinted with permission from Diebold, U., Applied Physics A-Materials Science & Processing, 2003. **76**(5): p. 681–687. Copyright Springer Science + Business Media, 2003.)

### 3.2. Kinetic and thermodynamic properties

Surface energy is a determining factor for the thermodynamic properties of micro-and nanoparticles. Nano-sized particles have higher surface areas, and thus greater surface energy. In an earlier

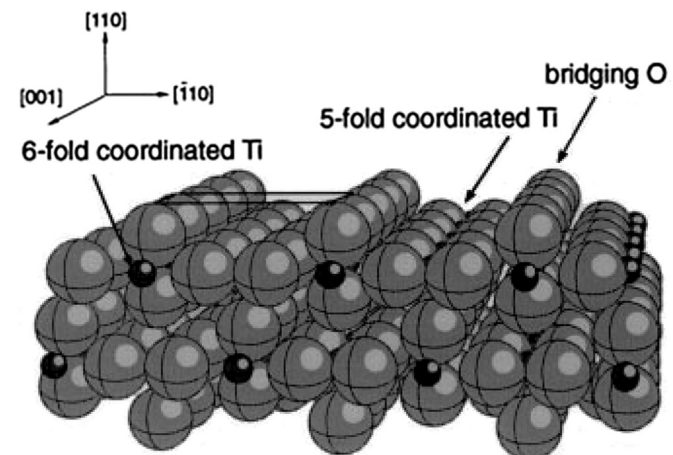


**Fig. 13.** Space-filling model of bulk terminated  $\text{TiO}_2(110)$  –  $(1 \times 1)$ . Small spheres represent  $\text{Ti}$  and large spheres represent  $\text{O}$  [62].

(Reprinted with permission from Charlton, G., P. Howes, C. Nicklin, P. Steadman, J. Taylor, C. Muryn, et al., Physical Review Letters, 1997. **78**(3): p. 495. Copyright American Chemical Society, 1997.)

**Table 2**

Surface atomic coordination and surface energy for several  $1 \times 1$  surfaces of different orientations [63].

Surface	Surface Ti coordination	Surface O coordination	Surface energy (meV/a.u. <sup>2</sup> ) (Unrelaxed)	Surface energy (meV/a.u. <sup>2</sup> ) (Relaxed)
(110)	5, 6	2, 3	30.7	15.6
(100)	5	2	33.8	19.6
(011)	5	2, 3	36.9	24.4
(001)	4	2	51.4	28.9

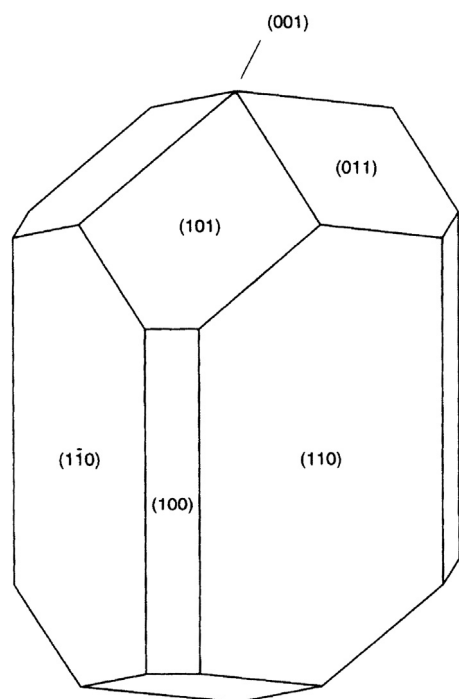


**Fig. 14.** The equilibrium shape of macroscopic crystals of rutile  $\text{TiO}_2$  using the Wulff construction [63].

(Reprinted with permission from Ramamoorthy, M., D. Vanderbilt, and R. King-Smith, Physical Review-Section B-Condensed Matter, 1994. **49**(23): p. 16721–16727. Copyright American Chemical Society, 1994.)

study, Mitsuhashi et al. [67] utilized high-temperature oxide melt solution calorimetry for determining the enthalpies of the brookite- and anatase-to-rutile phase transitions. The samples were single crystals of size 0.1–0.2 mm of anatase and natural brookite from Magnet Cove, Arkansas. The enthalpies of solution for the brookite-rutile and anatase-rutile transformations are  $-0.17 \pm 0.09$  kcal mol<sup>-1</sup> and  $-0.78 \pm 0.2$  kcal mol<sup>-1</sup>, respectively, at 971 K. The transformation enthalpies confirm that the relative stability sequence of the three polymorphs is rutile > anatase > brookite [67]. A stability reversal hysteresis of the anatase-rutile transformation is due to the higher surface energy of rutile compared to anatase [54,68,69]; rutile has more unsatisfied charges per unit surface area [40,52].

**Fig. 17** shows the free energy dependence on the particle size [54]. It was concluded from these data that relative phase stability depends on particle size, with the most stable phase being anatase at sizes less than 4.9 nm, brookite at sizes between 4.9 and 30 nm and rutile at sizes larger than 30 nm.

### 3.3. Electrical and optical properties

The electronic structure of  $\text{TiO}_2$  polymorphs has been studied experimentally by applying Auger electron spectroscopy (AES) [70,71], X-ray emission spectroscopy (XPS) [72,73], X-ray absorption spectroscopy (XAS) [74,75], electron energy loss spectroscopy (EELS) [74,76], resonant photoemission spectroscopy [75] and impedance spectroscopy [77].

In addition to experimental investigations, theoretical modeling is essential to understand the functional perspectives of  $\text{TiO}_2$  and its modifications. Theoretical studies of  $\text{TiO}_2$  polymorphs, especially rutile, have attracted a lot of attention. In an early study, Daude et al. [78,79] used the combination of the tight-binding approximation and pseudopotentials to calculate the electronic band structure of  $\text{TiO}_2$  for interpretation of experimental data [78,79]. Poumellet, Durham and Guo [80] studied the electronic band structure of rutile  $\text{TiO}_2$  by the linear muffin-tin orbital (LMTO) method [80]. Soft core ab initio pseudopotentials were also used with the local density approximation (LDA) to predict the electronic properties of rutile  $\text{TiO}_2$  [81]. Some other researchers used cluster methods, such as the embedded-cluster numerical discrete variational method, to calculate the band gap and density of states of rutile  $\text{TiO}_2$  [82,83]. Pseudopotential Hartree-Fock, ab-initio full-potential-linearized-augmented plane wave and self-consistent

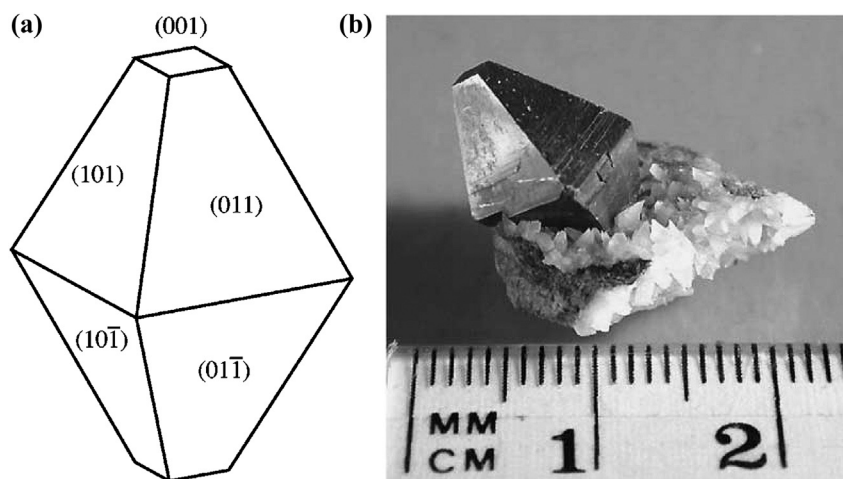


**Fig. 15.** (a) The equilibrium shape of a  $\text{TiO}_2$  crystal in the anatase phase, according to the Wulff construction and surface energies. (b) Picture of an anatase mineral crystal [25]. (Reprinted with permission from Lazzeri, M., A. Vittadini, and A. Selloni, Physical Review B, 2001. **63**(15): p. 155409. Copyright American Chemical Society, 2001.)

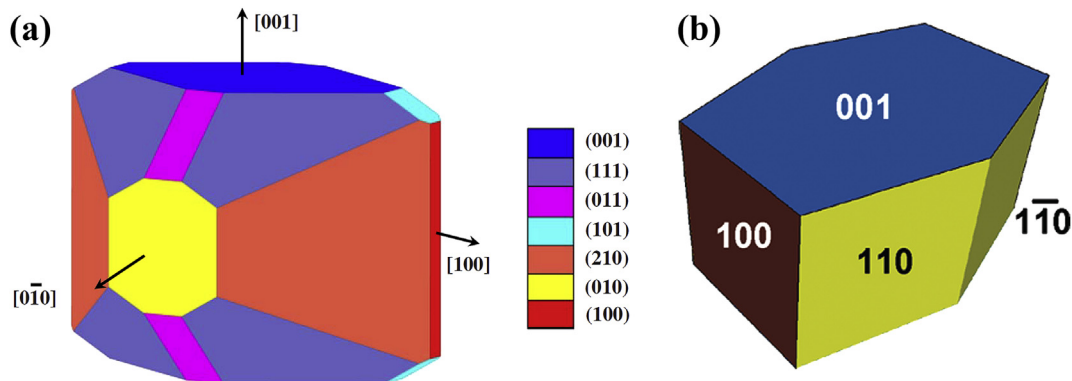


**Fig. 16.** Equilibrium shape of macroscopic (a) brookite [64]. (Reprinted with permission from Gong, X.-Q. and A. Selloni, Physical review B, 2007. **76**(23): p. 235307. Copyright American Chemical Society, 2007.) (b) TiO<sub>2</sub>(B) crystals using the Wulff construction and the surface energies [66]. (Reprinted with permission from Vittadini, A., M. Casarin, and A. Selloni, Journal of Materials Chemistry, 2010. **20**(28): p. 5871–5877. Copyright Royal Society of Chemistry, 2010.)

orthogonalized linear combination of atomic orbitals are some other methods using to calculate the electronic and optical properties of the TiO<sub>2</sub> polymorphs [84–87].

Although the theoretical studies are enormously useful for predicting and understanding the electronic properties of materials, the difficulty in accurately calculating the band structure of semiconductors and insulators leads to significant differences between theoretical and experimental results. Kohn-Sham density functional theory (DFT) and the Hartree-Fock (HF) are the most common methods for the prediction of the band structure of materials. DFT within the local density approximation (LDA) or even in the generalized gradient approximation (GGA) predicts a band gap for rutile, anatase and brookite of approximately one-third less than the experimental values ca. 3.0 eV. This reflects errors in the approximations as well as fundamental issues in using DFT to calculate band gaps [88].

There are two general methods to compensate for the underestimation of the band gap while using DFT. The first is to apply a self-interaction correction [89], the second is to utilize the many body (*GW*) approximation [90]. In the *GW* approximation, the many-body self-energy is approximated by the product of the single-particle Green function *G* and the screened interaction *W*. It is a numerically challenging theory, in part due to evaluation of the screening equation for *W* [91].

On the other hand, compared to DFT, HF theory generally overestimates band gaps. Thus, it has been proposed that the introduction of exact HF exchange into conventional DFT will improve the accuracy of the calculated band gap of TiO<sub>2</sub> [92,93]. The resulting approaches are known as “hybrid schemes”. Hybrid functionals used in band structure calculations include Becke’s three-parameter hybrid functional (B3LYP) which includes Becke’s three parameter exchange and Lee-Yang-Parr correlation [94,95]; PBE0, which mixes 25% of HF exchange with the PBE exchange-correlation functional [96,97]; HSE06 which mixes 20% of HF exchange with the HSE exchange-correlation functional [98–104].

Zhang et al. [105] studied the electronic structures of rutile, anatase and brookite with hybrid functional theory using various percentage contributions of HF exchange. Different theoretical approaches with different percentages of HF exchange alter the magnitude of the band gap, and the positions of the minima and maximum of the density of states. They showed that 13% HF exchange can correctly predict the electronic structures of rutile, anatase and brookite. Using the all electron basis sets of the Crystal Package with the threshold of total energy of 10<sup>-7</sup> a.u., hybrid functional with 13% HF exchange predicts a direct band gap for rutile at  $\Gamma$  and an indirect band gap from M to  $\Gamma$  for anatase, Fig. 18 [105]. The total and ion-decomposed electronic density of states of anatase and rutile using HSE06 are shown in Fig. 19. This figure shows that Ti<sub>3d</sub> states are the host of excess electrons and the electron holes centred on O<sub>2p</sub> states [106].

Labat et al. also studied the structural and electronic properties of TiO<sub>2</sub> polymorphs with PBE0 and B3LYP functionals, Fig. 20 [107]. There are O<sub>2s</sub> states around -18 eV, O<sub>2p</sub> states as topmost states of the valence band (VB) approximately -6 to 0 eV and Ti<sub>3d</sub> states above the Fermi level at the bottom of the conduction band. The valence band states are primarily formed from O<sub>2p</sub> states with non-negligible hybridization with Ti<sub>3d</sub> states. The conduction band is composed of both Ti<sub>3d</sub> and O<sub>2p</sub> states, but the contribution from Ti<sub>3d</sub> states is much more than from O<sub>2p</sub> states. Ti<sub>3d</sub> states contain the excess electrons whereas the electron holes will be centred on O<sub>2p</sub> states. A splitting of

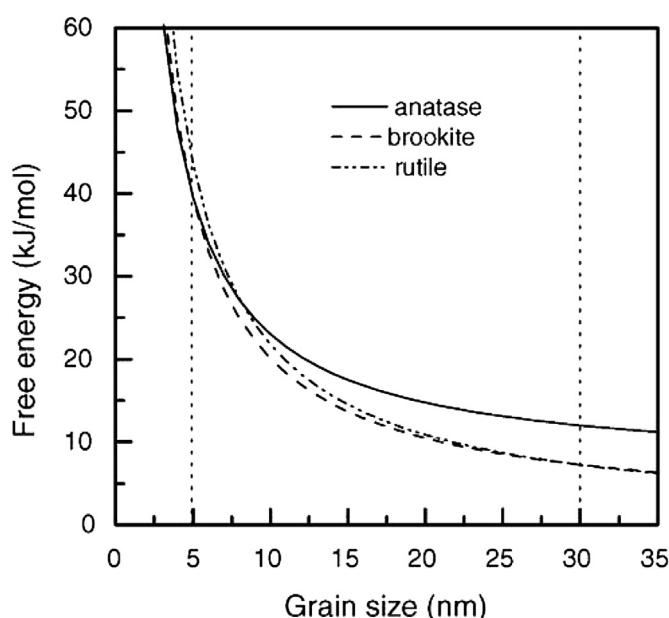


**Fig. 17.** Free energy vs. the grain size for anatase, brookite and rutile [54]. (Reprinted with permission from Zhu, K.-R., M.-S. Zhang, J.-M. Hong, and Z. Yin, Materials Science and Engineering A, 2005. **403**(1): p. 87–93. Copyright Elsevier, 2005.)

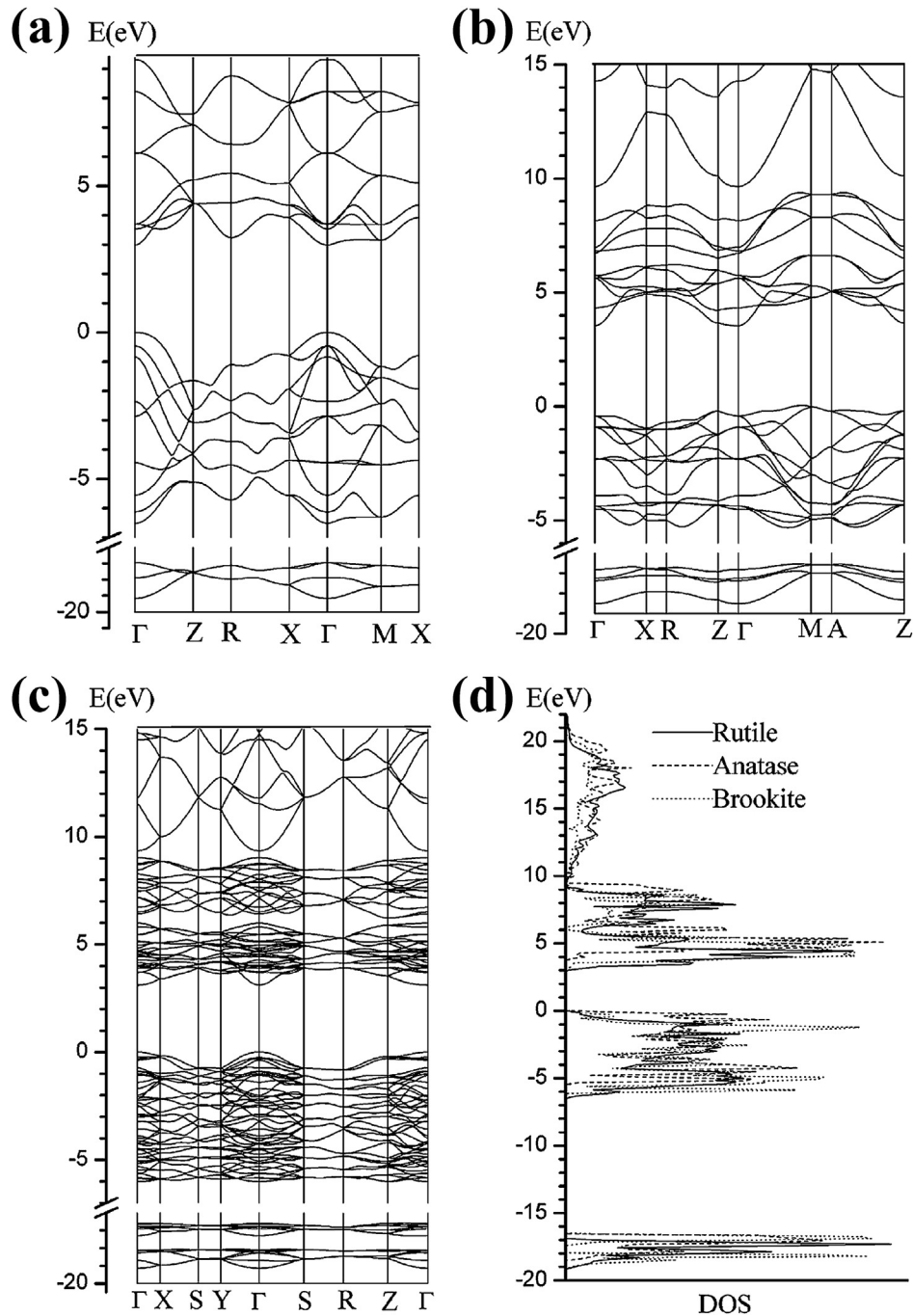


**Fig. 18.** Band structures of rutile (a), anatase (b), and brookite (c)  $\text{TiO}_2$  and total density of states (d) calculated by the hybrid DFT method with  $\delta = 13\%$ . The valence-band maximum is taken as the energy zero [105].

(Reprinted with permission from Yong-fan Zhang, W.L. Yi Li, Kai-ning Ding and Jun-qian Li, J. Phys. Chem. B, 2005. **109**: p. 19270–19277. Copyright American Chemical Society, 2005.)

the  $\text{O}_{2p}$  band was observed due to the bonding and antibonding  $\text{O}_{2p}$  states. Furthermore, because of the octahedral environment of Ti atoms,  $\text{Ti}_{3d}$  states split to  $\text{Ti} t_{2g}$  and  $\text{Ti} e_g$  states [106]. Studying the band structures of rutile and anatase shows the partially ionic behaviour of the Ti–O bond, and indicates that the covalent character of bonds is larger in rutile than anatase [107–109]. They used PWGGA (Perdew-Wang exchange-correlation functional) and PW1PW (DFT-HF hybrid) methods to predict the structure and electronic properties of rutile. Both methods show that rutile  $\text{TiO}_2$  is a direct-gap semiconductor. They used the highest symmetry points in

the Brillouin zone including  $Z \rightarrow A \rightarrow M \rightarrow \Gamma \rightarrow Z \rightarrow R \rightarrow X \rightarrow \Gamma$ . Their results showed that the smallest indirect gap of rutile structure is along the  $\Gamma \rightarrow M$  direction [108].

Ekuma et al. employed the LDA and LCAO to study the electronic and structural properties of rutile  $\text{TiO}_2$ . They solved the Kohn-Sham and the ground-state charge density equations self-consistently using the Bagayoko-Zhao-Williams (BZW) method [110–113]. The LDA-BZW calculations found an indirect band gap of 2.95 eV, from  $\Gamma \rightarrow R$  for rutile, and the calculated direct band gap of 3.05 at  $\Gamma$  is in good agreement with the experimental results [110].

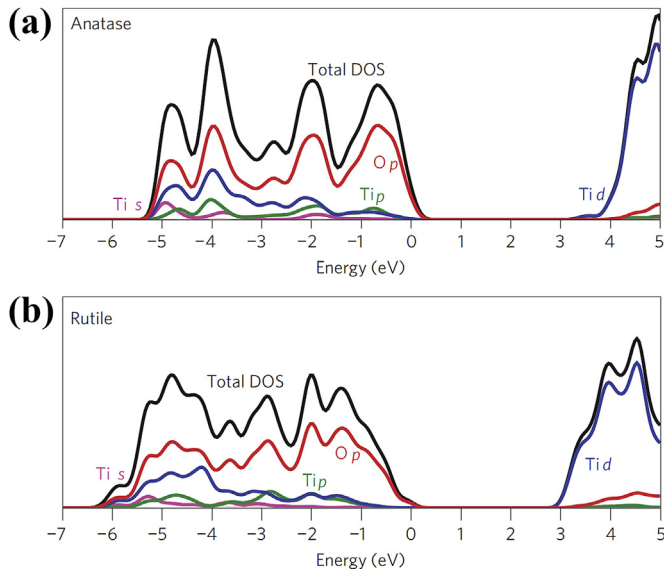


**Fig. 19.** The total and ion-decomposed electronic density of states of anatase (a) and rutile (b) using HSE06 [106].

(Reprinted with permission from Scanlon, D.O., C.W. Dunnill, J. Buckeridge, S.A. Shevlin, A.J. Logsdail, S.M. Woodley, et al., *Nature Materials*, 2013, **12**(9): p. 798–801. Copyright Nature Publishing Group, 2013.)

Landmann et al. [55] combined density functional theory and many-body perturbation theory to study the electronic and optical properties of  $\text{TiO}_2$  polymorphs. The obtained band structures for rutile, anatase and brookite are shown in Fig. 21. They used a modern nonlocal, range-separated, screened coulomb density functional proposed by Heyd-Scuseria and Ernzerhof (HSE06) [114,115] which compensates the underestimation of the band gap of  $\text{TiO}_2$  polymorphs compared to standard DFT [55,116].

Yun et al. used PBE and HSE06 methods for structural and density of states studies of anatase, rutile and fluorite phases. The results show that both methods correctly predict the structure of  $\text{TiO}_2$  polymorphs, but the screened hybrid DFT method improved the density of states and band gap energies of all polymorphs

[117,118]. Table 3 provides a comparison of calculated band gaps of different theoretical methods.

#### 4. Modifications

Research on modified  $\text{TiO}_2$  is mainly driven by the objective of narrowing the band gap to improve its photo reactivity under solar illumination. The description of producing new states in the band gap of semiconductors and the localized and delocalized nature of associated electrons is clearly an important challenge for understanding the properties of doped oxides [124]. Doping causes the production of vacancies, interstitial or substitutional defects which alter the colour, optical and magnetic properties, conductivity, reactivity etc. of doped oxides [125]. Doping titania with anions such as N, C, and S results in a red-shift of the absorption edge of the doped titanium dioxide, and so causes the absorption of the longer wavelengths in visible-light-active  $\text{TiO}_2$ .

##### 4.1. Noble metal loading

The deposition of a noble metal on semiconductor nanoparticles is an essential factor for maximizing the efficiency of photo catalytic reactions [126]. It is commonly assumed that the noble metal acts as a sink for photo-induced charge carriers and promotes interfacial charge transfer processes. Noble and semi-noble metals, including Pt, Au, Pd, Rh, Ni, Cu and Ag, have been reported to be very effective for enhancement of  $\text{TiO}_2$  photo catalysis [127–135]. As the Fermi levels of these noble metals are lower than that of  $\text{TiO}_2$ , photo-excited electrons can be transferred from the CB to metal particles deposited on the surface of  $\text{TiO}_2$ , while photo generated VB holes remain on the  $\text{TiO}_2$ . These activities greatly reduce the possibility of electron–hole recombination, resulting in efficient separation and stronger photo catalytic reactions [5]. Karakitsou et al. [136] showed that in the near-UV region (250–400 nm), Pt-doped anatase exhibits  $\text{H}_2$  production rates which are higher than those exhibited by the rutile form by a factor of approximately seven. They concluded that the efficiency of Pt/ $\text{TiO}_2$  photo catalysts is significantly affected by the crystallographic structure of  $\text{TiO}_2$ .

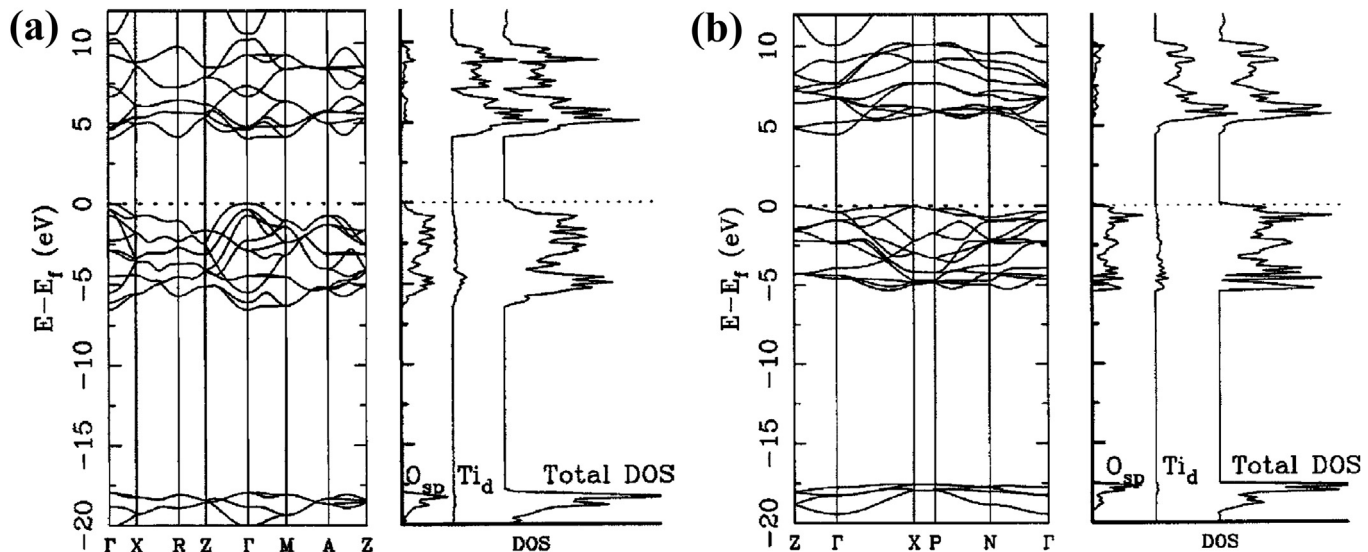


**Fig. 20.** Calculated band structure, total and projected DOS of  $\text{O}_{sp}$  and  $\text{Ti}_d$  of PBE0 method for (a) rutile and (b) anatase [107].

(Reprinted with permission from Labat, F., P. Baranek, C. Domain, C. Minot, and C. Adamo, *J Chem Phys*, 2007, **126**(15): p. 154703. Copyright American Institute of Physics, 2007.)

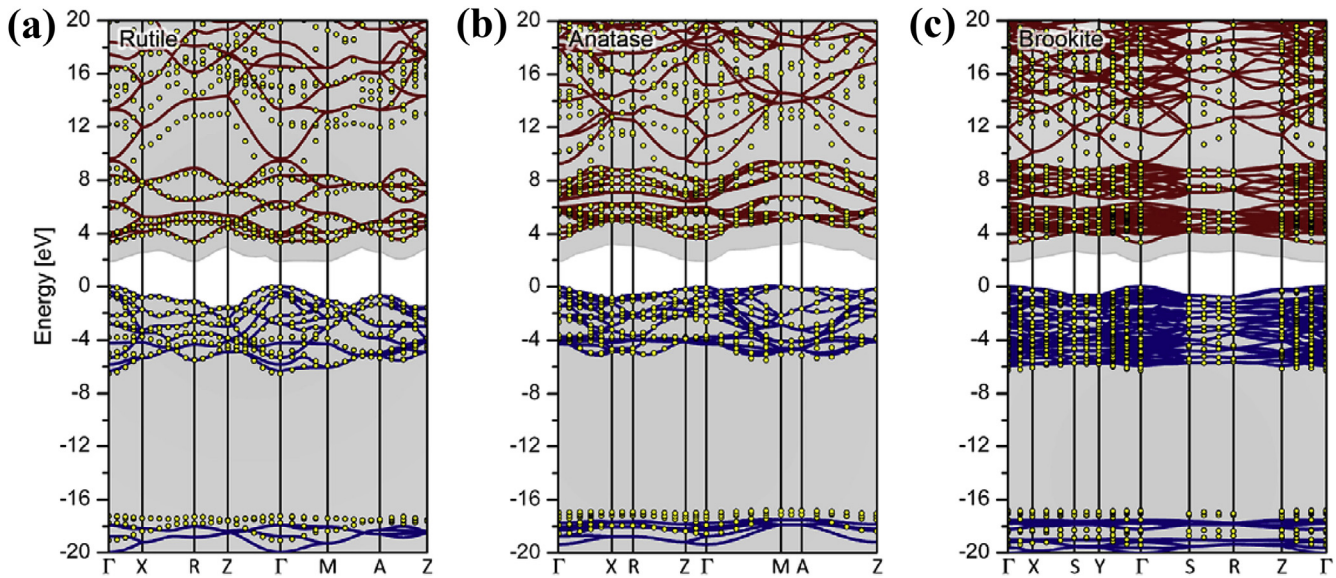


**Fig. 21.**  $\text{TiO}_2$  band structures for the rutile (a), anatase (b) and brookite (c) polymorphs in the HSE06, and quasiparticle (QP) energies (dots) obtained from PBE- $G_0W_0$  [55]. (Reprinted with permission from Landmann, M., E. Rauls, and W.G. Schmidt, J Phys Condens Matter, 2012. 24(19): p. 195503. Copyright IOP Publishing, 2012.)

#### 4.2. Ion doping

Doped  $\text{TiO}_2$  has different surface properties compared to pristine  $\text{TiO}_2$  including thickness of the space charge layer, existence and concentration of surface states [137]. Doping changes the

chemical nature and electronic structure of doped-oxide. The performance of  $\text{TiO}_2$  could be improved by band gap narrowing which leads to increased photoactivity in the visible spectral region. It was observed that the threshold photo energy for activating doped titania specimens changes which causes the red-

**Table 3**  
Comparison of the calculated band gaps of  $\text{TiO}_2$  with different methods.

Structure	Authors	Band gap $E_g$ (eV)	Method	Basis	Experimental value (eV)
Rutile	Labat et al. [107]	12.14 (D) 1.88 (D) 4.05 (D) 1.85 (D) 3.53 (D) 1.67 (D) 1.69 (D)	HF PBE PBE0 LDA LCAO B3LYP LDA PBE	LCAO	3.05 (I) [119]
	Poumellec et al. [80]	2.0 (I)	LDA	LMTO-ASA	
	Y. Zhang et al. [105]	2.99	HF-DFT ( $\delta = 13\%$ )	LCAO	
	Islam et al. [108]	1.9 (D)	DFT-GGA	LCAO	
	Ekuma et al. [110]	3.54 (D)	PW1PW DFT-HF		
	Landmann et al. [55]	3.05 (I) 1.88 (D) 3.39 (D) 3.46 (D) 3.73 (D)	BZW-LDA DFT-PBE HSE06 PBE0- $G_0W_0$ HSE06- $G_0W_0$	LCAO PAW PAW PAW	
		12.71 (I) 2.36 (I) 4.50 (I) 2.33 (I) 3.98 (I) 2.08 (I)	HF PBE PBE0 LDA B3LYP PBE	LCAO LCAO	3.18 (I) [102]
	Y. Zhang et al. [105]	3.54 (I)	HF-DFT ( $\delta = 13\%$ )	LCAO	
	Landmann et al. [55]	1.94 (I) 3.60 (I) 3.73 (I) 4.05 (I)	DFT-PBE DFT-HSE06 PBE0- $G_0W_0$ HSE06- $G_0W_0$	PAW PAW PAW PAW	
		1.86 (D) 3.30 (D) 3.45 (D) 4.68 (D) 3.11 (D)	DFT-PBE DFT-HSE06 PBE0- $G_0W_0$ HSE06- $G_0W_0$ HF-DFT ( $\delta = 13\%$ )	PAW PAW PAW PAW LCAO	

<sup>1</sup> PAW or a mix of PAW (for groundstate) and PW (for  $G_0W_0$ ) [120–123].

shifted adsorption edge to improve the photoreactivity properties of titania [138].

The enhancement or reduction of photo catalytic activity is explained in terms of alteration of the bulk electronic structure of the semiconductor, which in turn influences its electron–hole generation and separation capacity under illumination [139]. The position of the Fermi energy level, formation of new energy levels by the interaction of an interstitial dopant with the semiconductor lattice and the electrical conductivity of the semiconductor, also affects the surface properties such as thickness of the space charge layer, existence and concentration of surface states, and decomposition potentials which affect the photo corrosion process. Although disagreements occur in the literature as to the explanation of the red-shift of the absorption edge of doped TiO<sub>2</sub>, there is a consensus among researchers that oxygen vacancies and related colour centres are the most probable reasons for the improved photosensitivity [139,140].

#### 4.2.1. Cation-doped TiO<sub>2</sub>

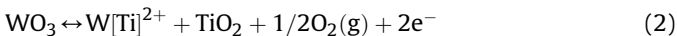
Since metal ions are incorporated into the TiO<sub>2</sub> lattice, impurity energy levels are formed in the band gap of TiO<sub>2</sub>. The energy level of electron traps should be below the CB edge, and the energy level of hole trap states should be below the VB edge. In the case of deep doping, metal ions most likely behave as recombination centres, since electron/hole transfer to the surface interface is more difficult [141].

Karakitsou et al. [136] worked on the influence of ultraviolet cation doping of TiO<sub>2</sub> on its performance as a photo catalyst in water cleavage applications. Anatase exhibits higher H<sub>2</sub> production rates compared to rutile. They concluded that doping with cations with higher valence, such as W<sup>6+</sup>, Ta<sup>5+</sup>, Nb<sup>5+</sup>, results in increasing the water cleavage rate, while doping with cations of lower valence such as In<sup>3+</sup>, Zn<sup>2+</sup>, Li<sup>+</sup> will cause reduction of the photocatalytic activity. Doping of TiO<sub>2</sub> with higher valence cations results in shifting the Fermi energy level towards negative values with respect to the NHE potential due to increasing the concentration of electrons in the conduction band. On the other hand, doping with lower valence cations causes increases in the concentration of holes in the valence band. In addition, the Fermi energy level is shifted to lower values, and the flat-band potential of TiO<sub>2</sub> is shifted toward positive values with respect to the NHE potential [136].

In addition, doping of TiO<sub>2</sub> with cations of valence higher than that of the parent Ti<sup>4+</sup> cation results in an increased concentration of electrons in the conduction band, as illustrated by the following defect site reactions:



or



Lowering of the work function (i.e. an upward shift of the Fermi energy level) is also expected, and consequently, a cathodic shift of the flat band potential toward negative values with respect to the NHE potential [136].

Choi et al. confirmed that the presence of metal ion dopants in the TiO<sub>2</sub> crystalline matrix significantly influences photo reactivity, charge carrier recombination rates, and interfacial electron-transfer rates. They concluded that doping with Fe<sup>3+</sup>, Mo<sup>5+</sup>, Ru<sup>3+</sup>, Os<sup>3+</sup>, Re<sup>5+</sup>, V<sup>4+</sup>, and Rh<sup>3+</sup> at 0.1–0.5 at.% significantly increases the photo reactivity for both oxidation and reduction while Co<sup>3+</sup> and Al<sup>3+</sup> doping decreases the photo reactivity [142–144].

Aluminium-doped rutile TiO<sub>2</sub> has been a focus of recent research [81,108,145] as well. Stoichiometric Al doping, along with

contributions from oxygen vacancies, slightly increases the band gap of rutile TiO<sub>2</sub>, and reduces the photo catalytic activity of titania pigments [81,108,145]. H doping of TiO<sub>2</sub> results in the reduction of Ti<sup>4+</sup> to Ti<sup>3+</sup> ions which are responsible for the accompanying increase of the electronic conductivity of TiO<sub>2</sub> by introducing localized or delocalized electronic states. Furthermore, there is debate as to whether oxygen vacancies or titanium interstitials are the dominant species in the n-doped TiO<sub>2</sub> [146,147]. DFT-U and hybrid B3LYP functional methods were used to characterize Ti<sup>3+</sup> interstitials. The study showed that different types of Ti<sup>3+</sup> centres with different degrees of localization and excitation energies control the electronic states of n-doped TiO<sub>2</sub> [146].

#### 4.2.2. Anion-doped TiO<sub>2</sub>

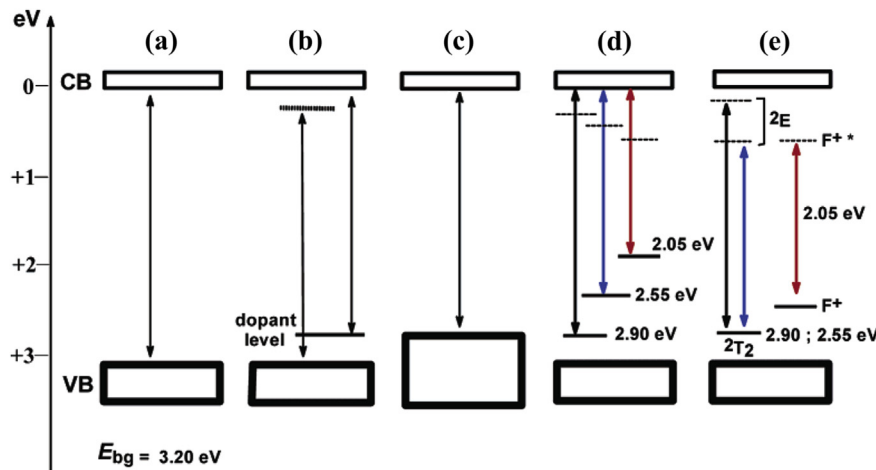
Recent research showed that cation doping causes localized *d* states deep in the band gap of TiO<sub>2</sub> and results in carrier recombination [148–150]. Unlike metal ions (cations), anions are less likely to form recombination centres and, therefore, are more effective in enhancing the photocatalytic activity. Doping titania with anions such as N, C, and S results in red-shift of the absorption edge. Asahi et al. [136] studied the visible-light-active photocatalytic properties of TiO<sub>2-x</sub>N<sub>x</sub> through first-principles calculations and x-ray photoemission spectroscopy. They concluded that nitrogen doping improves the optical absorption, photocatalytic activity such as photo-degradation of methylene blue and gaseous acetaldehyde and hydrophilicity of the film surface.

Fig. 22 b–e shows the predicted effects of doping on the band structure of anatase TiO<sub>2</sub>. Doping could cause the red-shift of the TiO<sub>2</sub> absorption edge by creating localized states and narrowing the band gap [150].

Valentin et al. investigated the influence on photo activity of anatase and rutile TiO<sub>2</sub> of substitutional N doping through DFT calculations. They showed that the N<sub>2p</sub> localized states just above the top of the O<sub>2p</sub> valence cause red shift and blue shift in anatase and rutile, respectively. The energy differences between the localized states and the conduction band of the both polymorphs for the pure and doped oxide are shown in Fig. 23 [151].

Many researchers have studied the defect structure (oxygen vacancies, Ti<sup>3+</sup> centres, etc.) of TiO<sub>2</sub> by theoretical analysis. Asahi et al. investigated the substitutional doping effects of C, N, F, P and S in anatase TiO<sub>2</sub>. They calculated the DOS of anion-doped anatase by the FLAPW formalism in the framework of LDA [149]. According to Fig. 24, nitrogen acts as the best dopant because of mixing its *p* states with O<sub>2p</sub> states which causes band-gap narrowing. It is worth mentioning that S has the same effect on band-gap narrowing as N, but the problem is that S doping has positive formation energy of 4.1 eV in comparison to 1.6 eV for the substitution of N in TiO<sub>2</sub>. Moreover, adding C and P will cause deep states in the band-gap which do not result in band-gap narrowing. In Fig. 24, N<sub>i</sub> and N<sub>i+s</sub> refer to interstitial N and both interstitial and substitutional doping in anatase. These states are unlikely to be effective for photocatalysis because they are well screened and hardly interact with the TiO<sub>2</sub> electronic states [149]. C-doped TiO<sub>2</sub> might exhibit new and unexpected features compared to N-doped TiO<sub>2</sub>. Nitrogen is roughly similar in size to oxygen and generally substitutes for the oxygen in the TiO<sub>2</sub> lattice. The valence shell of the C atom contains four electrons as does the Ti atom, but can also host up to four excess electrons [141,151,152].

Valentin et al. studied the effects of carbon doping on the visible light sensitivity of TiO<sub>2</sub>. They used DFT calculations within GGA for both anatase and rutile. They studied oxygen-poor and-rich oxygen for low and higher carbon concentrations. They concluded that substitutional (to oxygen) carbon and oxygen vacancies are favoured at low carbon concentrations and under oxygen-poor conditions, whereas, under oxygen rich conditions, interstitial and



**Fig. 22.** Various schemes illustrating the possible changes that might occur to the band gap electronic structure of anatase  $\text{TiO}_2$  on doping with various nonmetals: (a) band gap of pristine  $\text{TiO}_2$ ; (b) doped  $\text{TiO}_2$  with localized dopant levels near the VB and the CB; (c) band gap narrowing resulting from broadening of the VB; (d) localized dopant levels and electronic transitions to the CB; and (e) electronic transitions from localized levels near the VB to their corresponding excited states for  $\text{Ti}^{3+}$  and  $\text{F}^+$  centres [150]. (Reprinted with permission from Serpone, N., The Journal of Physical Chemistry B, 2006. **110**(48): p. 24287–24293. Copyright American Chemical Society, 2006.)

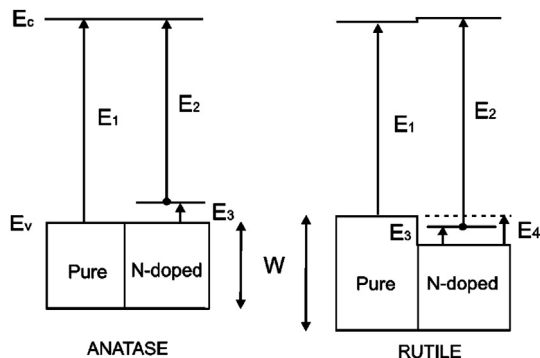


**Fig. 23.** Schematic representation of the band structure of pure and N-doped anatase and rutile. Energies are not in scale [151].

(Reprinted with permission from Di Valentin, C., G. Pacchioni, and A. Selloni, Physical Review B, 2004. **70**(8): p. 085116. Copyright American Chemical Society, 2004.)

substitutional (to Ti) C atoms are preferred. For higher carbon atom concentrations, an unexpected stabilization was seen because of multidoping effects, interpreted as inter-species redox processes. Carbon impurities produce several localized occupied states in the band gap causing red shift of the absorption edge [153].

#### 4.2.3. Oxygen-deficient $\text{TiO}_2$

The particular modification of  $\text{TiO}_2$  in which oxygen is removed, leaving a vacancy, is important and scientifically interesting. The general formula for reduced  $\text{TiO}_2$  is  $\text{TiO}_{2-x}$  which the value of  $x$  gives an estimate of the density of oxygen vacancies. Removal of more than a few percent of oxygen forms titanium sub oxides with the formula of  $\text{Ti}_n\text{O}_{2n-1}$ , with  $3 < n < 10$ :  $n \rightarrow \infty \equiv \text{TiO}_2$ , referred to as Magnéti phases. These have recently attracted considerable attention for their potential to improve the photocatalytic properties of  $\text{TiO}_2$ . Hydrogenation was used to produce Magnéti phase titanium sub-oxides in the 1950's for the first time.

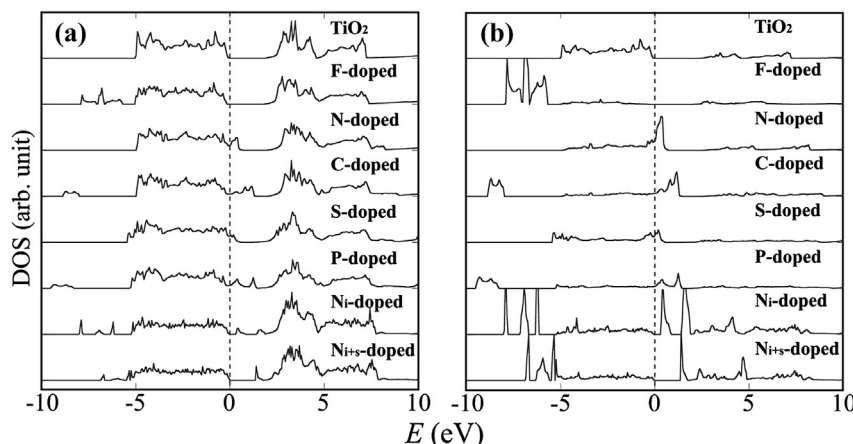


**Fig. 24.** (a) Total DOS of doped  $\text{TiO}_2$  and (b) the projected DOS into the doped anion sites, calculated by FLAPW. The dopants F, N, C, S, and P were located at a substitutional site for an O atom in the anatase  $\text{TiO}_2$  crystal (the eight  $\text{TiO}_2$  units per cell). The results for N doping at an interstitial site (Ni-doped) and that at both substitutional and interstitial sites (Ni<sub>1s</sub>-doped) are also shown [149].

(Reprinted with permission from Asahi, R., T. Morikawa, T. Ohwaki, K. Aoki, and Y. Taga, Science, 2001. **293**(5528): p. 269–271. Copyright American Association for the Advancement of Science, 2001.)

A companion review will be devoted to oxygen-deficient  $\text{TiO}_2$ . Here we give just two examples of a particular approach to introducing oxygen vacancies, viz reaction with hydrogen. Chen et al. [154] reported that by introduction of lattice disorder in hydrogenated anatase  $\text{TiO}_2$  nanocrystals, mid-gap electronic states are created which results in decreasing the band gap. Fig. 25 shows a schematic diagram of the density of states (DOS) of white (pristine) and black (H-modified) anatase. Experimentally, anatase turned black and improved its performance as Li-ion battery electrode.

Rutile can also be reduced under high pressure (around 40 bar) hydrogen and high temperature [155]. Rutile turns to blue during hydrogen at ion. Hydrogenated rutile nanorods were found experimentally to have superior performance compared to hydrogenated anatase nanoparticles in Li-ion battery electrodes.

#### 4.3. Ion implantation

It is thought that so called “second generation photocatalysts”, made by ion-engineering techniques, are the most effective for improving the photo catalytic properties of  $\text{TiO}_2$  by altering its electronic structure [148,156]. Bombardment of  $\text{TiO}_2$  with transition metal ions results in injection of these ions into the lattice and interaction with  $\text{TiO}_2$ . Yamashita et al. studied the photo catalytic properties of  $\text{TiO}_2$  implanted with  $\text{Cr}^+$  and  $\text{V}^+$ . The implantation process was conducted with an ion-implanter consisting of a metal ion source, mass analyser, high-voltage ion accelerator (150 keV) and a high vacuum pump [156]. They found that ion implantation resulted in a red shift in the absorption spectrum, leading to more effective decomposition of NO into  $\text{N}_2$ ,  $\text{O}_2$  and  $\text{N}_2\text{O}$  at 275 K in the visible light region [128]. The extent of the red shift depended on the metal ion implanted and its concentration. V, Cr, Mn, Fe and Ni caused a large shift in the absorption band of  $\text{TiO}_2$  toward the visible region. Al, Mg, or Ti implanted titanium oxides showed no shift, which means that red shift not only depends on the high energy implantation process, but also to the interaction of the implanted ions with the  $\text{TiO}_2$ . The order of the resulting increase in photocatalytic sensitivity was found to be  $\text{V} > \text{Cr} > \text{Mn} > \text{Fe} > \text{Ni}$  ions. Figs. 26 and 27 compose the UV-visible spectra of implanted and chemically doped with Cr ions [148].

Shown in Figs. 26 and 27, Anpo et al. [148], confirmed that only metal-ion implanted titanium oxide catalysts show shifts in the entire absorption band toward the visible light regions.

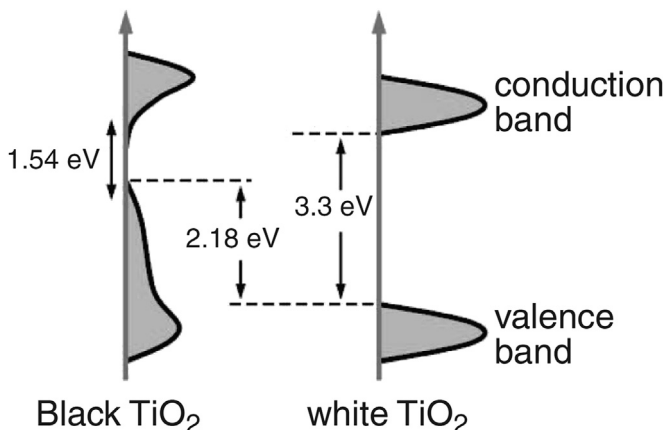


**Fig. 25.** Schematic illustration of the DOS of disorder-engineered black  $\text{TiO}_2$  nanocrystals, as compared to that of unmodified  $\text{TiO}_2$  nanocrystals [154].  
(Reprinted with permission from Chen, X., L. Liu, P.Y. Yu, and S.S. Mao, Science, 2011. 331(6018): p. 746–50. Copyright American Association for the Advancement of Science, 2011.)

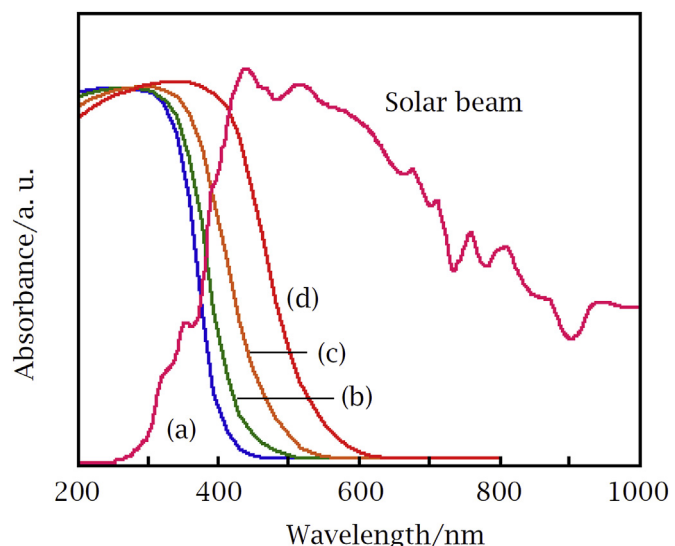


**Fig. 26.** Uv-Vis absorption spectra (diffuse reflectance) of the original unimplanted pure  $\text{TiO}_2$  (a) and the Cr ion implanted  $\text{TiO}_2$  (b–d), and the solar spectrum which reaches the earth. (amounts of Cr ion-implanted in  $10^{-7}$  mol/g, b: 2.2, c: 6.6, d: 13.0) [148].  
(Reprinted with permission from Anpo, M. and M. Takeuchi, Journal of Catalysis, 2003. 216(1): p. 505–516. Copyright Elsevier, 2003.)

The results obtained in photocatalytic reactions and various spectroscopic measurements carried out with the photocatalysts indicate that the implanted metal ions are highly dispersed within the deep bulk of the catalysts and work to modify their electronic nature without any changes in the chemical properties of the surfaces [148]. Yamashita et al. [157] also studied the visible light activity of transition metal implanted  $\text{TiO}_2$  using XAFS analysis and theoretical calculations. They concluded that the substitution of Ti ions by isolated metal ions is the determining factor for the utilization of solar light. Yamashita et al. also studied the properties of

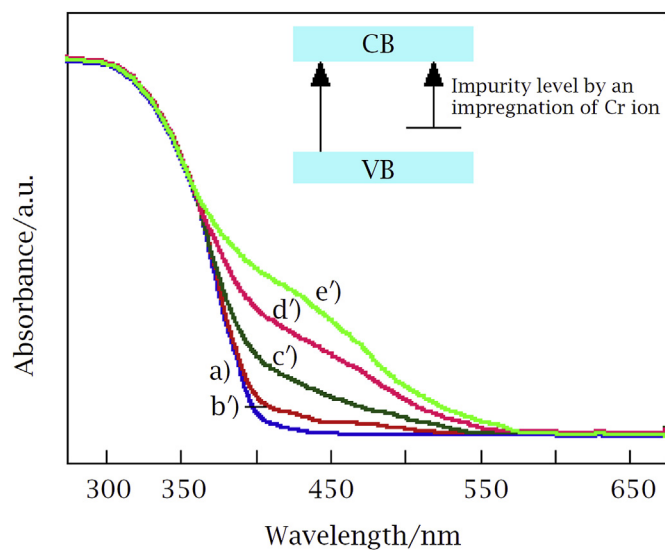


**Fig. 27.** Uv-Vis absorption spectra of (diffuse reflectance) of the original undoped pure  $\text{TiO}_2$  (a) and  $\text{TiO}_2$  chemically doped with Cr ions (b'–e'). (Cr ions chemically doped in  $10^{-7}$  mol/g, a: undoped original pure  $\text{TiO}_2$  (P-25), b': 16, c': 200, d': 1000, e': 2000) These  $\text{TiO}_2$  photo catalysts chemically doped with Cr ions did not exhibit any photo catalytic reactivity [148].  
(Reprinted with permission from Anpo, M. and M. Takeuchi, Journal of Catalysis, 2003. 216(1): p. 505–516. Copyright Elsevier, 2003.)

Fe ion-implanted TiO<sub>2</sub>, and found that the studied second type catalyst absorbs visible light in the range of 400–600 nm with an effective photocatalytic activity for water remediation. N-doped crystalline anatase in nanotube form is another promising photocatalyst with strongly enhanced photocurrent response to both UV and visible light [6].

## 5. Research progress in applications

### 5.1. UV absorption

A required feature of inorganic sunscreen filters is to screen/block UV light over the whole UV-A/UV-B range (290–400 nm) through absorption, scattering and reflection properties that in turn are influenced by the intrinsic refractive index, the size of the particles, dispersion in the emulsion base, and by their film thickness [5]. In addition to blocking UV radiation, sunscreens must be photostable (ideally 100%) and must dissipate the absorbed energy efficiently through photophysical and photochemical pathways that do not allow the formation of singlet oxygen, other reactive oxygen species, and other harmful reactive intermediates. With few exceptions, sunscreens contain chemical filters (organic; absorb mostly UVB radiation) and physical filters (e.g., TiO<sub>2</sub> and ZnO) [140]. Titanium dioxide, because of its high refractive index (2.90 for rutile) gives a high SPF. The rutile phase is generally used in sunscreen cosmetics because it is safer compared to anatase and anatase/rutile phases, which can be more harmful to the skin during oxidative reactions. Anatase and anatase/rutile adhere more strongly on skin, so washing of anatase is more difficult and damages the outer-most layer of the skin even in indoor light [158].

TiO<sub>2</sub> is effective against UV-B and gives reasonable protection in the UV-A range; it offers good transmission between 400 and 700 nm, enhanced by the reduction of the particle size to 10–20 nm, which achieves an optimal balance between scattering and absorption and provides excellent protection associated with satisfactory transparency.

The major disadvantage of inorganic sunscreens is that scattering extends into the visible region, causing a whitening effect, which is unappealing to the consumer. Many researchers have aimed to increase the visible transparency through superior control of particle size, shape and particle size distribution [4]. Popov et al. [159] evaluated the most appropriate size of TiO<sub>2</sub> nanoparticles. They concluded that particles of 62 nm are the most effective in protecting skin against UV-B light [159]. Recent studies, however, have shown that TiO<sub>2</sub> nanoparticles (NPs), usually a mixture of rutile and anatase, are not completely harmless to the human body and the toxic effects of TiO<sub>2</sub> particles are dose- and size-dependent [160,161]. When TiO<sub>2</sub> nanoparticles are photo-activated by UV light, they generate highly oxidizing radicals (OH and O<sub>2</sub><sup>·</sup>) and other reactive oxygen species (ROS) such as H<sub>2</sub>O<sub>2</sub> and singlet oxygen, O<sub>2</sub>, which are known to be cytotoxic and/or genotoxic [5]. For example, on the human skin, 20-nm TiO<sub>2</sub> NPs are photoactive, producing free radicals that might cause the complete destruction of supercoiled skin cell DNA, even at low doses and in the absence of exposure to UV [160].

Recent work on improving the properties of TiO<sub>2</sub> for use in sunscreens has focused on nano-sized particles. A surface coating can be added to nano-sized TiO<sub>2</sub>, commercial TiO<sub>2</sub> (P25) powder, to enhance its UV absorption by a different light diffraction mechanism. Composites consisting of nano-sized particle TiO<sub>2</sub> in SiO<sub>2</sub> gels have been synthesized enhancing the UV absorption efficiency, the major factor for UV protection [11].

### 5.2. Photocatalysis

Transition-metal ions in photocatalytic reactions have attracted a lot of attention for two main reasons: (a) their influence on the rate of reaction (mainly oxidation) and (b) the transformation of the ions to less toxic species or their deposition on a semiconductor catalyst surface for recovery of expensive and useful metals.

TiO<sub>2</sub> has been utilized in numerous aspects of photocatalysis, including water dissociation, air/water remediation, removal of indoor odours, antibacterial applications and self-cleaning surfaces. TiO<sub>2</sub> has photo-induced superhydrophilicity properties as well.

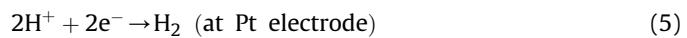
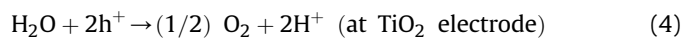
The ratio of the surface charge carrier transfer rate to the electron–hole (e<sup>-</sup>/h<sup>+</sup>) recombination rate is the determining factor for evaluating the photocatalytic activity of titanium oxide. Particle size is also one of the most important factors affecting the surface activity of the catalyst. With decreasing particle size, the specific surface area and surface active sites will increase, but it should be noticed that there is an optimal particle size of around 10 nm in which the particle has the highest surface activity. Zhang et al. claimed that for particle sizes less than 10 nm, the surface recombination rate increases, so the catalytic activity will decrease. Thus, there should be compatibility between particle size, surface activity and recombination centres to have the most efficient photocatalyst [162].

Due to the thermodynamic stability of anatase nanoparticles with crystal sizes below ca. 11 nm relative to brookite and rutile, and the ease of their synthesis, they are commonly employed in TiO<sub>2</sub> photocatalysis. On the other hand, it was reported that brookite nanocrystals exhibit markedly high photocatalytic activities compared to those of rutile and anatase. Kandiel et al. [163,164] studied the photocatalytic activities of anatase, rutile and brookite through photooxidation of methanol. They observed that brookite nanoparticles have higher photocatalytic activities than anatase, and a comparable activity to that of the anatase-rich nanoparticles. Interestingly, the photocatalytic activity of anatase is much higher than that of TiO<sub>2</sub>(B), but the electronic band gap of TiO<sub>2</sub>(B) is narrower than that of anatase [163,164]. Yang et al. [165] proposed mixed-phase nanofibres for photocatalytic applications, consisting of a shell of anatase nanocrystals on a fibril core of single-crystal TiO<sub>2</sub>(B). The well-matched and stable phase interfaces cause the better holes migration to the core phase. On the other hand, the anatase shell has a high ability to absorb oxygen. As a result, these two phenomena decrease the recombination rate [165].

#### 5.2.1. Photocatalytic water splitting

Research on photoelectrocatalytic properties of TiO<sub>2</sub> was boosted in the 1970's by Fujishima and co-workers [33], who showed that TiO<sub>2</sub> could be utilized as an electrode in a photoelectrolytic cell to produce clean hydrogen through water splitting [166]. The electrochemical photocell consists of two electrodes, the TiO<sub>2</sub> photocatalyst as the anode and Pt as the counter electrode. When TiO<sub>2</sub> electrode is irradiated with light which wavelength is compatible to the band gap of TiO<sub>2</sub>, the photo-generated electrons and holes are produced [167]. The schematic diagram of a photoelectrochemical cell is shown in Fig. 28.

The photocatalytic reactions of TiO<sub>2</sub> are as follows:



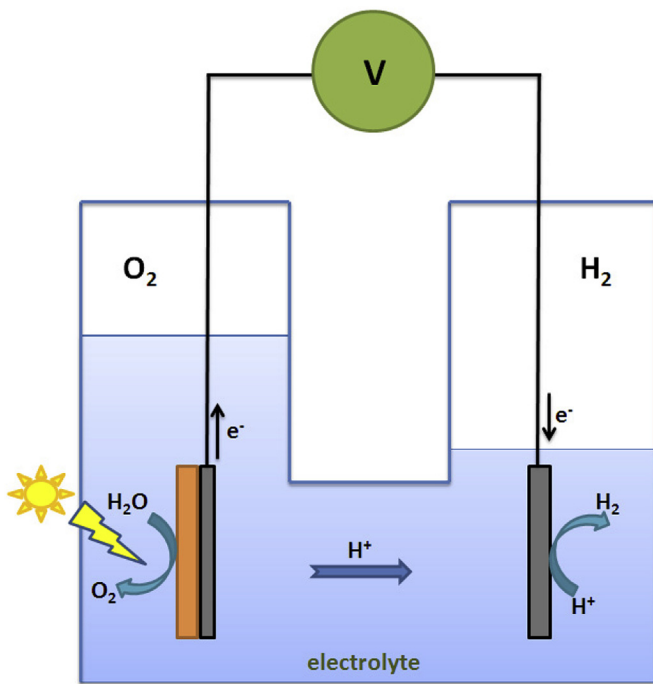


**Fig. 28.** Schematic diagram of a photoelectrochemical cell [30].

(Reprinted with permission from Ahmad, H., S.K. Kamarudin, L.J. Minggu, and M. Kassim, Renewable and Sustainable Energy Reviews, 2015. 43: p. 599–610. Copyright Elsevier, 2015.)

The overall reaction is:



For hydrogen production, the CB level should be more negative on the electrochemical scale than the hydrogen evolution potential ( $E_{\text{H}_2/\text{H}_2\text{O}}$ ) to flow electrons from the semiconductor surface to the counter electrode, while the VB should be more positive than the water oxidation level ( $E_{\text{O}_2/\text{H}_2\text{O}}$ ) for efficient oxygen production without an applied potential. Fig. 29 demonstrates the basic principle of the overall water–dissociation reaction on a solid semiconductor photocatalyst [168,169].

The solar energy conversion efficiency of TiO<sub>2</sub> for photocatalytic water splitting is still low mainly due to the recombination of photo-generated electron/hole pairs, fast backward reaction and

rather high band gap [170]. Adding electron donors or acceptors helps to enhance the photo-generated electron/hole separation, resulting in reducing the recombination rate. As mentioned in sections 4.2 and 4.3, band gap engineering of TiO<sub>2</sub>, using cation/anion doping and ion implantation, reduces the recombination rate and allows TiO<sub>2</sub> photocatalyst to absorb the visible light [138,149,153,171–175].

## 6. Summary

Titanium-dioxide is a wide band-gap semiconductor, with the principal polymorphs (rutile, anatase, brookite) having measured band-gaps in the range 3.05–3.18 eV. The functional performance of TiO<sub>2</sub> is fundamentally determined by its band structure, which is sensitive to crystal structure and changes to the stoichiometry or chemical identity of the constituent atoms. This ability to tune the electronic properties has led to an ongoing research effort to enhance the electrochemical properties in particular.

The crystal structures of the four known polymorphs and (where known) their thermodynamic properties, optical properties and band structures were surveyed. Particular attention was paid to the prediction of the band structures of the pure polymorphs, since this must be robust before reliable calculations of the effects of vacancies, doping and so on can be performed. Density functional theory, which performs very poorly in predicting the energetics of semiconductors in the common local density approximation, is nevertheless fairly reliable overall with judicious choice of a hybrid functional.

Close attention was also paid to the thermodynamics of TiO<sub>2</sub> nanoparticles, since the optical properties are strongly size-dependent and the order of stability of the polymorphs at macroscopic size is upset for nanoparticles, as are their relative activities in photocatalysis.

Numerous modifications by surface loading with metals, doping and introduction of oxygen vacancies were surveyed. Predictions of the effect on band structure of these modifications are more qualitative, generally revolving around the introduction of new states within the band gap rather than narrowing of the gap itself. There is a need for the latest methods to be applied to more quantitative predictions of the effects of structural and chemical modifications on the electronic structure.

Finally, recent progress in applications including UV screening, photocatalysis and water splitting were surveyed. The most significant scientific problem associated with TiO<sub>2</sub> is still to substantially increase the fraction of the solar spectrum that can be captured as a photocurrent.

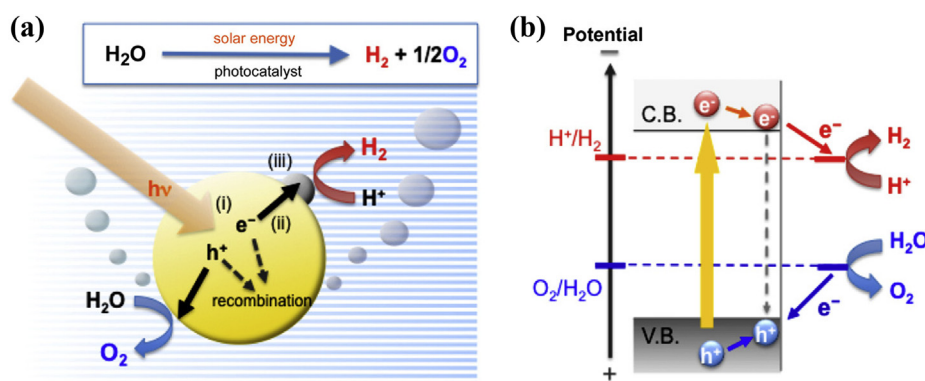


**Fig. 29.** Schematic diagram showing (a) the mechanism and (b) the potentials for water splitting occurring on the TiO<sub>2</sub> surface [169].

(Reprinted with permission from Abe, R., Journal of Photochemistry and Photobiology C: Photochemistry Reviews, 2010. 11(4): p. 179–209 Copyright Elsevier, 2010.)

## References

- [1] Cava RJ, DiSalvo FJ, Brus LE, Dunbar KR, Gorman CB, Haile SM, et al. Future directions in solid state chemistry: report of the NSF-sponsored workshop. *Prog solid state Chem* 2002;30(1):1–101.
- [2] Gázquez MJ, Bolívar JP, García-Tenorio R, Vaca F. A review of the production cycle of titanium dioxide pigment. *Mater Sci Appl* 2014;05(07):441–58.
- [3] Robichaud CO, Uyar AE, Darby MR, Zucker LG, Wiesner MR. Estimates of upper bounds and trends in nano-TiO<sub>2</sub> production as a basis for exposure assessment. *Environ Sci Technol* 2009;43(12):4227–33.
- [4] Dransfield G. Inorganic sunscreens. *Radiat Prot Dosim* 2000;91(1–3):271–3.
- [5] Serpone N, Dondi D, Albini A. Inorganic and organic UV filters: their role and efficacy in sunscreens and skincare products. *Inorganica Chim Acta* 2007;360(3):794–802.
- [6] Yamashita H, Harada M, Misaka J, Takeuchi M, Neppolian B, Anpo M. Photocatalytic degradation of organic compounds diluted in water using visible light-responsive metal ion-implanted TiO<sub>2</sub> catalysts: Fe ion-implanted TiO<sub>2</sub>. *Catal Today* 2003;84(3–4):191–6.
- [7] Bard AJ. Design of semiconductor photoelectrochemical systems for solar energy conversion. *J Phys Chem* 1982;86(2):172–7.
- [8] Choi HC, Ahn H-J, Jung YM, Lee MK, Shin HJ, Kim SB, et al. Characterization of the structures of size-selected TiO<sub>2</sub> nanoparticles using X-ray absorption spectroscopy. *Appl Spectrosc* 2004;58(5):598–602.
- [9] Xiaobo C. Titanium dioxide nanomaterials and their energy applications. *Chin J Catal* 2009;30(8):839–51.
- [10] Şennik E, Çolak Z, Kılıç N, Öztürk ZZ. Synthesis of highly-ordered TiO<sub>2</sub> nanotubes for a hydrogen sensor. *Int J Hydrogen Energy* 2010;35(9):4420–7.
- [11] Jaroenworaluck A, Pijarn N, Kosachan N, Stevens R. Nanocomposite TiO<sub>2</sub>–SiO<sub>2</sub> gel for UV absorption. *Chem Eng J* 2012;181:45–55.
- [12] Mor GK, Varghese OK, Paulose M, Ong KG, Grimes CA. Fabrication of hydrogen sensors with transparent titanium oxide nanotube-array thin films as sensing elements. *Thin Solid Films* 2006;496(1):42–8.
- [13] Mattesini M, De Almeida J, Dubrovinsky L, Dubrovinskaia N, Johansson B, Ahuja R. High-pressure and high-temperature synthesis of the cubic TiO<sub>2</sub> polymorph. *Phys Rev B* 2004;70(21):212101.
- [14] Swamy V, Muddle BC. Ultrastiff cubic TiO<sub>2</sub> identified via first-principles calculations. *Phys Rev Lett* 2007;98(3):035502.
- [15] Koči L, Kim DY, de Almeida JS, Mattesini M, Isaev E, Ahuja R. Mechanical stability of TiO<sub>2</sub> polymorphs under pressure: ab initio calculations. *J Phys Condens Matter* 2008;20(34):345218.
- [16] Dewhurst J, Lowther J. High-pressure structural phases of titanium dioxide. *Phys Rev B* 1996;54(6):R3673.
- [17] Liang Y, Zhang B, Zhao J. Mechanical properties and structural identifications of cubic TiO<sub>2</sub>. *Phys Rev B* 2008;77(9):094126.
- [18] Dubrovinskaia NA, Dubrovinsky LS, Ahuja R, Prokopenko VB, Dmitriev V, Weber H-P, et al. Experimental and theoretical identification of a new high-pressure TiO<sub>2</sub> polymorph. *Phys Rev Lett* 2001;87(27):275501.
- [19] Nishio-Hamane D, Shimizu A, Nakahira R, Niwa K, Sano-Furukawa A, Okada T, et al. The stability and equation of state for the cotunnite phase of TiO<sub>2</sub> up to 70 GPa. *Phys Chem Miner* 2009;37(3):129–36.
- [20] Zhou X-F, Dong X, Qian G-R, Zhang L, Tian Y, Wang H-T. Unusual compression behavior of TiO<sub>2</sub> polymorphs from first principles. *Phys Rev B* 2010;82(6):060102.
- [21] Sato H, Endo S, Sugiyama M, Kikegawa T, Shimomura O, Kusaba K. Baddeleyite-type high-pressure phase of TiO<sub>2</sub>. *Science* 1991;251(4995):786–8.
- [22] Muscat J, Swamy V, Harrison NM. First-principles calculations of the phase stability of TiO<sub>2</sub>. *Phys Rev B* 2002;65(22):224112.
- [23] Gerward L, Staun Olsen J. Post-rutile high-pressure phases in TiO<sub>2</sub>. *J Appl Crystallogr* 1997;30(3):259–64.
- [24] Shannon RD, Pask JA. Kinetics of the anatase–rutile transformation. *J Am Ceram Soc* 1965;48(8):391–8.
- [25] Lazzeri M, Vittadini A, Selloni A. Structure and energetics of stoichiometric TiO<sub>2</sub> anatase surfaces. *Phys Rev B* 2001;63(15):155409.
- [26] Marchand R, Brohan L, Tournoux M. TiO<sub>2</sub> (B) a new form of titanium dioxide and the potassium octatitanate K<sub>2</sub>Ti<sub>8</sub>O<sub>17</sub>. *Mater Res Bull* 1980;15(8):1129–33.
- [27] Banfield JF, Veblen DR, Smith DJ. The identification of naturally occurring TiO<sub>2</sub> (B) by structure determination using high-resolution electron microscopy, image simulation, and distance-least-squares refinement. *Am Mineral* 1991;76(3–4):343–53.
- [28] Armstrong AR, Armstrong G, Canales J, Bruce PG. TiO<sub>2</sub>-B nanowires. *Angew Chem Int Ed* 2004;43(17):2286–8.
- [29] Fujishima A. Electrochemical photolysis of water at a semiconductor electrode. *nature* 1972;238:37–8.
- [30] Ahmad H, Kamarudin SK, Minggu IJ, Kassim M. Hydrogen from photocatalytic water splitting process: a review. *Renew Sustain Energy Rev* 2015;43:599–610.
- [31] Diebold U. The surface science of Titanium Dioxide. *Surf Sci Rep* 2003;58:53–229.
- [32] Carp O, Huisman CL, Reller A. Photoinduced reactivity of titanium dioxide. *Prog solid state Chem* 2004;32(1):33–177.
- [33] Fujishima A, Zhang X, Tryk D. TiO<sub>2</sub> photocatalysis and related surface phenomena. *Surf Sci Rep* 2008;63(12):515–82.
- [34] Cassaignon S, Koelsch M, Jolivet J-P. Selective synthesis of brookite, anatase and rutile nanoparticles: thermolysis of TiCl<sub>4</sub> in aqueous nitric acid. *J Mater Sci* 2007;42(16):6689–95.
- [35] Li G, Li L, Boerio-Goates J, Woodfield BF. High purity anatase TiO<sub>2</sub> nanocrystals: near room-temperature synthesis, grain growth kinetics, and surface hydration chemistry. *J Am Chem Soc* 2005;127(24):8659–66.
- [36] Mahshid S, Ghamsari MS, Askari M, Afshar N, Lahuti S. Synthesis of TiO<sub>2</sub> nanoparticles by hydrolysis and peptization of titanium isopropoxide solution. *Semicond Phys Quantum Electron Optoelectron* 2006;9(2):65–8.
- [37] Hulteen J. A general template-based method for the preparation of nanomaterials. *J Mater Chem* 1997;7(7):1075–87.
- [38] Huczko A. Template-based synthesis of nanomaterials. *Appl Phys Mater Sci Process* 2000;70(4):365–76.
- [39] Kasuga T, Hiramatsu M, Hoson A, Sekino T, Niihara K. Formation of titanium oxide nanotube. *Langmuir* 1998;14(12):3160–3.
- [40] Banfield J. Thermodynamic analysis of phase stability of nanocrystalline titania. *J Mater Chem* 1998;8(9):2073–6.
- [41] Ding X-Z, Liu X-h. Correlation between anatase-to-rutile transformation and grain growth in nanocrystalline titania powders. *J Mater Res* 1998;13(09):2556–9.
- [42] Ranade M, Navrotsky A, Zhang H, Banfield J, Elder S, Zaban A, et al. Energetics of nanocrystalline TiO<sub>2</sub>. *Proc Natl Acad Sci* 2002;99(suppl 2):6476–81.
- [43] Ye X, Sha J, Jiao Z, Zhang L. Thermoanalytical characteristic of nanocrystalline brookite-based titanium dioxide. *Nanostructured Mater* 1997;8(7):19–27.
- [44] Mehranpour H, Askari M, Ghamsari MS, Farzalibeik H. Study on the phase transformation kinetics of sol-gel derived TiO<sub>2</sub> nanoparticles. *J Nanomat* 2010;2010:31.
- [45] Reyes-Coronado D, Rodriguez-Gattorno G, Espinosa-Pesqueira M, Cab C, De Coss R, Osakan G. Phase-pure TiO<sub>2</sub> nanoparticles: anatase, brookite and rutile. *Nanotechnology* 2008;19(14):145605.
- [46] Ocana M, Garcia-Ramos JV, Serna CJ. Low-temperature nucleation of rutile observed by Raman Spectroscopy during crystallization of TiO<sub>2</sub>. *J Am Ceram Soc* 1992;75(7):2010–2.
- [47] Swamy V, Muddle BC, Dai Q. Size-dependent modifications of the Raman spectrum of rutile TiO<sub>2</sub>. *Appl Phys Lett* 2006;89(16):3118.
- [48] Wang JW, Mishra AK, Zhao Q, Huang LP. Size effect on thermal stability of nanocrystalline anatase TiO<sub>2</sub>. *J Phys Appl Phys* 2013;46(25):255303.
- [49] Humin Cheng JM, Zhao Zhenguo, Qi Limin. Hydrothermal preparation of uniform nanosize rutile and anatase particles. *Chem Mater* 1995;7:663–71.
- [50] Tompsett G, Bowmaker G, Cooney R, Metson J, Rodgers K, Seakins J. The Raman spectrum of brookite, TiO<sub>2</sub> (PBCA, Z=8). *J Raman Spectrosc* 1995;26(1):57–62.
- [51] Iliev M, Hadjiev V, Litvinchuk A. Raman and infrared spectra of brookite (TiO<sub>2</sub>): experiment and theory. *Vib Spectrosc* 2013;64:148–52.
- [52] Zhang H, Banfield JF. Understanding polymorphic phase transformation behavior during growth of nanocrystalline aggregates: insights from TiO<sub>2</sub>. *J Phys Chem B* 2000;104(15):3481–7.
- [53] Zhang J, Li MJ, Feng ZC, Chen J, Li C. UV Raman spectroscopic study on TiO<sub>2</sub>. I. Phase transformation at the surface and in the bulk. *J Phys Chem B* 2006;110(2):927–35.
- [54] Zhu K-R, Zhang M-S, Hong J-M, Yin Z. Size effect on phase transition sequence of TiO<sub>2</sub> nanocrystal. *Mater Sci Eng A* 2005;403(1):87–93.
- [55] Landmann M, Rauls E, Schmidt WG. The electronic structure and optical response of rutile, anatase and brookite TiO<sub>2</sub>. *J Phys Condens Matter* 2012;24(19):195503.
- [56] Dylla AG, Henkelman G, Stevenson KJ. Lithium insertion in nanostructured TiO<sub>2</sub> (B) architectures. *Acc Chem Res* 2013;46(5):1104–12.
- [58] Cromer DT, Herrington K. The structures of anatase and rutile. *J Am Chem Soc* 1955;77(18):4708–9.
- [59] Tracy L, Thompson John T, Yates J. Surface science studies of the photoactivation of TiO<sub>2</sub>-new photochemical processes. *Chem Rev* 2006;106:4428–53.
- [60] Thompson TL, Yates JT. TiO<sub>2</sub>-based photocatalysis: surface defects, oxygen and charge transfer. *Top Catal* 2005;35(3–4):197–210.
- [61] Diebold U. Structure and properties of TiO<sub>2</sub> surfaces: a brief review. *Appl Phys Mater Sci Process* 2003;76(5):681–7.
- [62] Charlton G, Howes P, Nicklin C, Steadman P, Taylor J, Muryn C, et al. Relaxation of TiO<sub>2</sub>(110)-(1×1) using surface X-ray diffraction. *Phys Rev Lett* 1997;78(3):495.
- [63] Ramamoorthy M, Vanderbilt D, King-Smith R. First-principles calculations of the energetics of stoichiometric TiO<sub>2</sub> surfaces. *Phys Review-Section Condens Matter* 1994;49(23):16721–7.
- [64] Gong X-Q, Selloni A. First-principles study of the structures and energetics of stoichiometric brookite TiO<sub>2</sub> surfaces. *Phys Rev B* 2007;76(23):235307.
- [65] Kobayashi M, Kato H, Kakihana M. Synthesis of titanium dioxide nanocrystals with controlled crystal-and micro-structures from titanium complexes. *Nanomater Nanotechnol* 2013;3:1–10.
- [66] Vittadini A, Casarin M, Selloni A. Hydroxylation of TiO<sub>2</sub>-B: insights from density functional calculations. *J Mater Chem* 2010;20(28):5871–7.
- [67] Mitsuhashi T, Kleppa O. Transformation enthalpies of the TiO<sub>2</sub> polymorphs. *J Am Ceram Soc* 1979;62(7–8):356–7.
- [68] Navrotsky A, Kleppa O. Enthalpy of the anatase–rutile transformation. *J Am Ceram Soc* 1967;50(11):626–626.

- [69] Satoh N, Nakashima T, Yamamoto K. Metastability of anatase: size dependent and irreversible anatase-rutile phase transition in atomic-level precise titania. *Sci Rep* 2013;3:1959.
- [70] Göpel W, Anderson J, Frankel D, Jaehnig M, Phillips K, Schäfer J, et al. Surface defects of  $\text{TiO}_2(110)$ : a combined XPS, XAES and ELS study. *Surf Sci* 1984;139(2):333–46.
- [71] Hüner S, Wertheim GK. X-ray photoelectron band structure of some transition-metal compounds. *Phys Rev B* 1973;8(10):4857–67.
- [72] Finkelstein L, Kurmaev EZ, Korotin M, Moewes A, Schneider B, Butorin S, et al. Band approach to the excitation-energy dependence of x-ray fluorescence of  $\text{TiO}_2$ . *Phys Rev B* 1999;60(4):2212.
- [73] Woicik J, Nelson E, Kronik L, Jain M, Chelikowsky JR, Heskett D, et al. Hybridization and bond-orbital components in site-specific X-ray photoelectron spectra of rutile  $\text{TiO}_2$ . *Phys Rev Lett* 2002;89(7):077401.
- [74] De Groot F, Faber J, Michiels J, Czyzak M, Abbate M, Fuglie J. Oxygen 1s X-ray absorption of tetravalent titanium oxides: a comparison with single-particle calculations. *Phys Rev B* 1993;48(4):2074.
- [75] Thomas A, Flavell W, Mallick A, Kumarasinghe A, Tsoutsou D, Khan N, et al. Comparison of the electronic structure of anatase and rutile  $\text{TiO}_2$  single-crystal surfaces using resonant photoemission and x-ray absorption spectroscopy. *Phys Rev B* 2007;75(3):035105.
- [76] Brydson R, Sauer H, Engel W, Hofer F. Electron energy-loss near-edge structures at the oxygen K edges of titanium (IV) oxygen compounds. *J Phys Condens Matter* 1992;4(13):3429.
- [77] Weibel A, Bouchet R, Knauth P. Electrical properties and defect chemistry of anatase ( $\text{TiO}_2$ ). *Solid State Ion* 2006;177(3):229–36.
- [78] Goringe C, Bowler D, Hernandez E. Tight-binding modelling of materials. *Rep Prog Phys* 1997;60(12):1447.
- [79] Daude N, Gout C, Jouanin C. Electronic band structure of titanium dioxide. *Phys Rev B* 1977;15(6):3229–35.
- [80] Poumellec B, Durham PJ, Guo GY. Electronic-structure and X-ray absorption-spectrum of rutile  $\text{TiO}_2$ . *J Physics-Condensed Matter* 1991;3(42):8195–204.
- [81] Glassford KM, Chelikowsky JR. Structural and electronic properties of titanium dioxide. *Phys Rev B* 1992;46(3):1284.
- [82] Hagfeldt A, Siegbahn H, Lindquist SE, Lunell S. Semiempirical calculations of  $\text{TiO}_2$  (rutile) clusters. *Int J Quantum Chem* 1992;44(4):477–95.
- [83] Lin L, Mo S, Lin D. Electronic structure of rutile ( $\text{TiO}_2$ ). *J Phys Chem Solids* 1993;54(8):907–12.
- [84] Mo S-D, Ching W. Electronic and optical properties of three phases of titanium dioxide: rutile, anatase, and brookite. *Phys Rev B* 1995;51(19):13023.
- [85] Fahmi A, Minot C, Silvi B, Causá M. Theoretical analysis of the structures of titanium dioxide crystals. *Phys Rev B* 1993;47(18):11717–24.
- [86] Hafner J. Ab-initio simulations of materials using VASP: density-functional theory and beyond. *J Comput Chem* 2008;29(13):2044–78.
- [87] Vogtenhuber D, Podlucky R, Neckel A, Steinemann SG, Freeman AJ. Electronic structure and relaxed geometry of the  $\text{TiO}_2$  rutile (110) surface. *Phys Rev B* 1994;49(3):2099–103.
- [88] Janotti A, Varley J, Rinke P, Umezawa N, Kresse G, Van de Walle C. Hybrid functional studies of the oxygen vacancy in  $\text{TiO}_2$ . *Phys Rev B* 2010;81(8):085212.
- [89] Perdew JP, Zunger A. Self-interaction correction to density-functional approximations for many-electron systems. *Phys Rev B* 1981;23(10):5048–79.
- [90] Morgan BJ, Watson GW. A DFT+U description of oxygen vacancies at the  $\text{TiO}_2$  rutile (110) surface. *Surf Sci* 2007;601(21):5034–41.
- [91] Hedin L. New method for calculating the one-particle Green's Function with application to the electron-gas problem. *Phys Rev* 1965;139(3A):796–823.
- [92] Lee N-H, Oh H-J, Jung S-C, Lee W-J, Kim D-H, Kim S-J. Photocatalytic properties of nanotubular-shaped  $\text{TiO}_2$  powders with anatase phase obtained from titanate nanotube powder through various thermal treatments. *Int J Photoenergy* 2011;2011:1–7.
- [93] Nolan M, Long R, English NJ, Mooney DA. Hybrid density functional theory description of N- and C-doping of NiO. *J Chem Phys* 2011;134(22):224703.
- [94] Lee C, Yang W, Parr RG. Development of the Colle-Salvetti correlation-energy formula into a functional of the electron density. *Phys Rev B* 1988;37(2):785–9.
- [95] Becke AD. Density-functional thermochemistry. III. The role of exact exchange. *J Chem Phys* 1993;98(7):5648.
- [96] Perdew JP, Ernzerhof M, Burke K. Rationale for mixing exact exchange with density functional approximations. *J Chem Phys* 1996;105(22):9982.
- [97] Adamo C, Barone V. Toward reliable density functional methods without adjustable parameters: the PBE0 model. *J Chem Phys* 1999;110(13):6158.
- [98] Heyd J, Scuseria GE, Ernzerhof M. Hybrid functionals based on a screened Coulomb potential. *J Chem Phys* 2003;118(18):8207–15.
- [99] Heyd J, Scuseria GE. Assessment and validation of a screened Coulomb hybrid density functional. *J Chem Phys* 2004;120(16):7274–80.
- [100] Muscat J, Wander A, Harrison N. On the prediction of band gaps from hybrid functional theory. *Chem Phys Lett* 2001;342(3):397–401.
- [101] Heyd J, Scuseria GE. Efficient hybrid density functional calculations in solids: assessment of the Heyd-Scuseria-Ernzerhof screened Coulomb hybrid functional. *J Chem Phys* 2004;121(3):1187–92.
- [102] de PR Moreira I, Illas F, Martin RL. Effect of Fock exchange on the electronic structure and magnetic coupling in NiO. *Phys Rev B* 2002;65(15):155102.
- [103] Heyd J, Peralta JE, Scuseria GE, Martin RL. Energy band gaps and lattice parameters evaluated with the Heyd-Scuseria-Ernzerhof screened hybrid functional. *J Chem Phys* 2005;123(17):174101.
- [104] Peralta JE, Heyd J, Scuseria GE, Martin RL. Spin-orbit splittings and energy band gaps calculated with the Heyd-Scuseria-Ernzerhof screened hybrid functional. *Phys Rev B* 2006;74(7):073101.
- [105] Yong-fan Zhang WL, Li Yi, Ding Kai-ning, Li Jun-qian. A theoretical study on the electronic structures of  $\text{TiO}_2$ : effect of Hartree-Fock exchange. *J Phys Chem B* 2005;109:19270–7.
- [106] Scanlon DO, Dunnill CW, Buckeridge J, Shevlin SA, Logsdail AJ, Woodley SM, et al. Band alignment of rutile and anatase  $\text{TiO}_2$ . *Nat Mater* 2013;12(9):798–801.
- [107] Labat F, Baranek P, Domain C, Minot C, Adamo C. Density functional theory analysis of the structural and electronic properties of  $\text{TiO}_2$  rutile and anatase polytypes: performances of different exchange-correlation functionals. *J Chem Phys* 2007;126(15):154703.
- [108] Islam MM, Bredow T, Gerson A. Electronic properties of oxygen-deficient and aluminum-doped rutile  $\text{TiO}_2$  from first principles. *Phys Rev B* 2007;76(4):045217.
- [109] Asahi R, Taga Y, Mannstadt W, Freeman A. Electronic and optical properties of anatase  $\text{TiO}_2$ . *Phys Rev B* 2000;61(11):7459.
- [110] Ekuma CE, Bagayoko D. Ab-initio electronic and structural properties of rutile titanium dioxide. *Jpn J Appl Phys* 2011;50(10):101103.
- [111] Magyari-Köpe B, Park SG, Lee H-D, Nishi Y. First principles calculations of oxygen vacancy-ordering effects in resistance change memory materials incorporating binary transition metal oxides. *J Mater Sci* 2012;47(21):7498–514.
- [112] Ekuma EC, Franklin L, Zhao GL, Wang JT, Bagayoko D. Ab-initio local density approximation description of the electronic properties of zinc blende cadmium sulfide (zb-CdS). *Phys B Condens Matter* 2011;406(8):1477–80.
- [113] Harmon BN, Weber W, Hamann DR. Total-energy calculations for Si with a first-principles linear-combination-of-atomic-orbitals method. *Phys Rev B* 1982;25(2):1109–15.
- [114] Moussa JE, Schultz PA, Chelikowsky JR. Analysis of the Heyd-Scuseria-Ernzerhof density functional parameter space. *J Chem Phys* 2012;136(20):204117.
- [115] Hummer K, Harl J, Kresse G. Heyd-Scuseria-Ernzerhof of hybrid functional for calculating the lattice dynamics of semiconductors. *Phys Rev B* 2009;80(11):115205.
- [116] Vydrov OA, Heyd J, Kruckau AV, Scuseria GE. Importance of short-range versus long-range Hartree-Fock exchange for the performance of hybrid density functionals. *J Chem Phys* 2006;125(7):074106.
- [117] Wang Y, Hwang GS. Adsorption of Au atoms on stoichiometric and reduced  $\text{TiO}_2(110)$  rutile surfaces: a first principles study. *Surf Sci* 2003;542(1–2):72–80.
- [118] Yun Wang HZ, Liu Porun, Yaob Xiangdong, Zhao Huijun. Engineering the band gap of bare titanium dioxide materials for visible-light activity: a theoretical prediction. *RSC Adv* 2013;3:8777–82.
- [119] Nowotny M, Bak T, Nowotny J. Electrical properties and defect chemistry of  $\text{TiO}_2$  single crystal. I. Electrical conductivity. *J Phys Chem B* 2006;110(33):16270–82.
- [120] Shishkin M, Marsman M, Kresse G. Accurate quasiparticle spectra from self-consistent GW calculations with vertex corrections. *Phys Rev Lett* 2007;99(24):246403.
- [121] Shishkin M, Marsman M, Kresse G. Accurate quasiparticle spectra from self-consistent GW calculations with vertex corrections. *Phys Rev Lett* 2007;99(24):246403.
- [122] Fuchs F, Furthmüller J, Bechstedt F, Shishkin M, Kresse G. Quasiparticle band structure based on a generalized Kohn-Sham scheme. *Phys Rev B* 2007;76(11):115109.
- [123] Shishkin M, Kresse G. Self-consistent GW calculations for semiconductors and insulators. *Phys Rev B* 2007;75(23).
- [124] Ganduglia-Pirovano MV, Hofmann A, Sauer J. Oxygen vacancies in transition metal and rare earth oxides: current state of understanding and remaining challenges. *Surf Sci Rep* 2007;62(6):219–70.
- [125] Finazzi E, Di Valentini C, Pacchioni G, Selloni A. Excess electron states in reduced bulk anatase  $\text{TiO}_2$ : comparison of standard GGA, GGA+U, and hybrid DFT calculations. *J Chem Phys* 2008;129(15):154113.
- [126] Bumajdad A, Madkour M. Understanding the superior photocatalytic activity of noble metals modified titania under UV and visible light irradiation. *Phys Chem Chem Phys* 2014;16(16):7146–58.
- [127] Papp J, Shen H, Kershaw R, Dwight K, Wold A. Titanium (IV) oxide photocatalysts with palladium. *Chem Mater* 1993;5(3):284–8.
- [128] Adachi K, Ohta K, Mizuno T. Photocatalytic reduction of carbon dioxide to hydrocarbon using copper-loaded titanium dioxide. *Sol Energy* 1994;53(2):187–90.
- [129] Wu N-L, Lee M-S. Enhanced  $\text{TiO}_2$  photocatalysis by Cu in hydrogen production from aqueous methanol solution. *Int J Hydrogen Energy* 2004;29(15):1601–5.
- [130] Waterhouse G, Wahab A, Al-Oufi M, Jovic V, Anjum DH, Sun-Waterhouse D, et al. Hydrogen production by tuning the photonic band gap with the electronic band gap of  $\text{TiO}_2$ . *Sci Rep* 2013;3:2849.
- [131] Nada A, Barakat M, Hamed H, Mohamed N, Veziroglu T. Studies on the photocatalytic hydrogen production using suspended modified  $\text{TiO}_2$  photocatalysts. *Int J Hydrogen Energy* 2005;30(7):687–91.

- [132] Matthey D, Wang J, Wendt S, Matthiesen J, Schaub R, Lægsgaard E, et al. Enhanced bonding of gold nanoparticles on oxidized TiO<sub>2</sub>(110). *Science* 2007;315(5819):1692–6.
- [133] Sakthivel S, Shankar M, Palanichamy M, Arabindoo B, Bahnemann D, Murugesan V. Enhancement of photocatalytic activity by metal deposition: characterisation and photonic efficiency of Pt, Au and Pd deposited on TiO<sub>2</sub> catalyst. *Water Res* 2004;38(13):3001–8.
- [134] Tsydenov DE, Parmon VN, Vorontsov AV. Toward the design of asymmetric photocatalytic membranes for hydrogen production: preparation of TiO<sub>2</sub>-based membranes and their properties. *Int J Hydrogen Energy* 2012;37(15):11046–60.
- [135] Liu S, Qu Z, Han X, Sun C. A mechanism for enhanced photocatalytic activity of silver-loaded titanium dioxide. *Catal Today* 2004;93:877–84.
- [136] Karakitsou KE, Verykios XE. Effects of altervalent cation doping of titania on its performance as a photocatalyst for water cleavage. *J Phys Chem* 1993;97(6):1184–9.
- [137] Zaleska A. Doped-TiO<sub>2</sub>: a review. *Recent Pat Eng* 2008;2:157–64.
- [138] Kuznetsov VN, Serpone N. On the origin of the spectral bands in the visible absorption spectra of visible-light-active TiO<sub>2</sub> specimens analysis and assignments. *J Phys Chem C* 2009;113(34):15110–23.
- [139] Choi J, Park H, Hoffmann MR. Effects of single metal-ion doping on the visible-light photoreactivity of TiO<sub>2</sub>. *J Phys Chem C* 2009;114(2):783–92.
- [140] Daghbir R, Drogui P, Robert D. Modified TiO<sub>2</sub> for environmental photocatalytic applications: a review. *Ind Eng Chem Res* 2013;52(10):3581–99.
- [141] Banerjee AN. The design, fabrication, and photocatalytic utility of nanostructured semiconductors: focus on TiO<sub>2</sub>-based nanostructures. *Nano-technol Sci Appl* 2011;4:35–65.
- [142] Wonyong Choi AT, Hoffmann Michael R. The role of metal ion dopants in quantum-sized TiO<sub>2</sub>: correlation between photoreactivity and charge carrier recombination dynamics. *J Phys Chem* 1994;98:13669–79.
- [143] Jina Choi HPaMRH. Effects of single metal-ion doping on the visible-light photoreactivity of TiO<sub>2</sub>. *J Phys Chem C* 2010;114:783–92.
- [144] Kubacka A, Fernández-García M, Colón G. Advanced nanoarchitectures for solar photocatalytic applications. *Chem Rev* 2011;112(3):1555–614.
- [145] Janotti A, Van de Walle CG. LDA + U and hybrid functional calculations for defects in ZnO, SnO<sub>2</sub>, and TiO<sub>2</sub>. *Phys Status Solidi (b)* 2011;248(4):799–804.
- [146] Di Valentin C, Pacchioni G, Selloni A. Reduced and n-type doped TiO<sub>2</sub>: nature of Ti<sup>3+</sup> species. *J Phys Chem C* 2009;113(48):20543–52.
- [147] Finazzi E, Di Valentin C, Pacchioni G. Nature of Ti interstitials in reduced bulk anatase and rutile TiO<sub>2</sub>. *J Phys Chem C* 2009;113(9):3382–5.
- [148] Anpo M, Takeuchi M. The design and development of highly reactive titanium oxide photocatalysts operating under visible light irradiation. *J Catal* 2003;216(1):505–16.
- [149] Asahi R, Morikawa T, Ohwaki T, Aoki K, Taga Y. Visible-light photocatalysis in nitrogen-doped titanium oxides. *Science* 2001;293(5528):269–71.
- [150] Serpone N. Is the band gap of pristine TiO<sub>2</sub> narrowed by anion-and cation-doping of titanium dioxide in second-generation photocatalysts? *J Phys Chem B* 2006;110(48):24287–93.
- [151] Di Valentin C, Pacchioni G, Selloni A. Origin of the different photoactivity of N-doped anatase and rutile TiO<sub>2</sub>. *Phys Rev B* 2004;70(8):085116.
- [152] Di Valentin C, Finazzi E, Pacchioni G, Selloni A, Livraghi S, Paganini MC, et al. N-doped TiO<sub>2</sub>: theory and experiment. *Chem Phys* 2007;339(1–3):44–56.
- [153] Di Valentin C, Pacchioni G, Selloni A. Theory of carbon doping of titanium dioxide. *Chem Mater* 2005;17(26):6656–65.
- [154] Chen X, Liu L, Yu PY, Mao SS. Increasing solar absorption for photocatalysis with black hydrogenated titanium dioxide nanocrystals. *Science* 2011;331(6018):746–50.
- [155] Qiu J, Li S, Gray E, Liu H, Gu Q-F, Sun C, et al. Hydrogenation synthesis of blue TiO<sub>2</sub> for high-performance lithium-ion batteries. *J Phys Chem C* 2014;118(17):8824–30.
- [156] Yamashita H, Harada M, Misaka J, Nakao H, Takeuchi M, Anpo M. Application of ion beams for preparation of TiO<sub>2</sub> thin film photocatalysts operable under visible light irradiation: ion-assisted deposition and metal ion-implantation. *Nucl Instrum Methods Phys Res Sect B Beam Interact Mater Atoms* 2003;206:889–92.
- [157] Yamashita H, Harada M, Misaka J, Takeuchi M, Ichihashi Y, Goto F, et al. Application of ion beam techniques for preparation of metal ion-implanted TiO<sub>2</sub> thin film photocatalyst available under visible light irradiation: metal ion-implantation and ionized cluster beam method. *J Synchrotron Radiat* 2001;8(Pt 2):569–71.
- [158] Turci F, Peira E, Corazzari I, Fenoglio I, Trotta M, Fubini B. Crystalline phase modulates the potency of nanometric TiO<sub>2</sub> to adhere to and perturb the stratum corneum of porcine skin under indoor light. *Chem Res Toxicol* 2013;26(10):1579–90.
- [159] Popov A, Priesshev A, Lademann J, Myllylä R. TiO<sub>2</sub> nanoparticles as an effective UV-B radiation skin-protective compound in sunscreens. *J Phys D Appl Phys* 2005;38(15):2564.
- [160] Contado C, Pagnoni A. TiO<sub>2</sub> in commercial sunscreen lotion: flow field-flow fractionation and ICP-AES together for size analysis. *Anal Chem* 2008;80(19):7594–608.
- [161] Chang X, Zhang Y, Tang M, Wang B. Health effects of exposure to nano-TiO<sub>2</sub>: a meta-analysis of experimental studies. *Nanoscale Res Lett* 2013;8(1):1–10.
- [162] Zhang Z, Wang C-C, Zakaria R, Ying JY. Role of particle size in nanocrystalline TiO<sub>2</sub>-based photocatalysts. *J Phys Chem B* 1998;102(52):10871–8.
- [163] Kandiel TA, Robben L, Alkaim A, Bahnemann D. Brookite versus anatase TiO<sub>2</sub> photocatalysts: phase transformations and photocatalytic activities. *Photochem Photobiol Sci* 2013;12(4):602–9.
- [164] Kandiel TA, Feldhoff A, Robben L, Dillert R, Bahnemann DW. Tailored titanium dioxide nanomaterials: anatase nanoparticles and Brookite nanorods as highly active photocatalysts. *Chem Mater* 2010;22(6):2050–60.
- [165] Yang DJ, Liu HW, Zheng ZF, Yuan Y, Zhao JC, Waclawik ER, et al. An efficient photocatalyst structure: TiO<sub>2</sub>(B) nanofibers with a shell of anatase nanocrystals. *J Am Chem Soc* 2009;131(49):17885–93.
- [166] Fujishima A, Zhang X. Titanium dioxide photocatalysis: present situation and future approaches. *Comptes Rendus Chim* 2006;9(5):750–60.
- [167] Hashimoto K, Irie H, Fujishima A. TiO<sub>2</sub> photocatalysis: a historical overview and future prospects. *Jpn J Appl Phys* 2005;44(12):8269–85.
- [168] Navarro Yerga RM, Alvarez Galvan MC, del Valle F, Villoria de la Mano JA, Fierro JL. Water splitting on semiconductor catalysts under visible-light irradiation. *ChemSusChem* 2009;2(6):471–85.
- [169] Abe R. Recent progress on photocatalytic and photoelectrochemical water splitting under visible light irradiation. *J Photochem Photobiol C Photochem Rev* 2010;11(4):179–209.
- [170] Ni M, Leung MKH, Leung DYC, Sumathy K. A review and recent developments in photocatalytic water-splitting using TiO<sub>2</sub> for hydrogen production. *Renew Sustain Energy Rev* 2007;11(3):401–25.
- [171] Vračar LM, Krstajić N, Radmilović V, Jakšić M. Electrocatalysis by nanoparticles–oxygen reduction on Ebonex/Pt electrode. *J Electroanal Chem* 2006;587(1):99–107.
- [172] Zhang D, Yang M, Dong S. Hydroxylation of the rutile TiO<sub>2</sub> (110) surface enhancing its reducing power for photocatalysis. *J Phys Chem C* 2015;119(3):1451–6.
- [173] Seferlis AK, Kollia M, Neophytides SG. The in situ electrochemical stable promotion of photoelectrocatalytic activity of TiO<sub>2</sub> by pulsed reductive doping: application in photoelectrochemical water splitting. *J Electrochem Soc* 2015;162(6):H397–402.
- [174] Tiido K, Alexeyeva N, Couillard M, Bock C, MacDougall BR, Tammeveski K. Graphene–TiO<sub>2</sub> composite supported Pt electrocatalyst for oxygen reduction reaction. *Electrochimica Acta* 2013;107:509–17.
- [175] Cho Y-J, Kim H-i, Lee S, Choi W. Dual-functional photocatalysis using a ternary hybrid of TiO<sub>2</sub> modified with graphene oxide along with Pt and fluoride for H<sub>2</sub>-producing water treatment. *J Catal* 2015;330:387–95.